Size-dependent protein segregation creates a spatial switch for Notch and APP signaling

Minsuk Kwak[1,2,3,4,5,6,*], Kaden M. Southard[1,2,*], Nam Hyeong Kim[1,2,3,6], Ramu Gopalappa[4,8], Woon Ryoung Kim[1,2,3], Minji An[4,5], Hyun Jung Lee[1,2,3], Justin Farlow[2], Anastasios Georgakopoulos[9], Nikolaos K. Robakis[9], Daeha Seo[10], Hyeong Bum Kim[4,5,8,11,12], Yong Ho Kim[6,7], Jinwoo Cheon[4,5,13], Zev J. Gartner[2,14,†] , Young-wook Jun[1,2,3,4,5†]

[1]Department of Otolaryngology, University of California, San Francisco, CA, USA
[2]Department of Pharmaceutical Chemistry, University of California, San Francisco, CA, USA
[3]Helen Diller Family Cancer Comprehensive Center (HDFCCC), University of California, San Francisco, CA, USA
[4]Center for Nanomedicine, Institute for Basic Science (IBS), Seoul, Republic of Korea
[5]Graduate Program of Nano Biomedical Engineering (Nano BME), Advanced Science Institute, Yonsei University, Seoul, Republic of Korea
[6]SKKU Advanced Institute of Nanotechnology (SAINT), Sungkyunkwan University, Suwon, Republic of Korea
[7]Department of Biomedical Engineering, Sungkyunkwan University, Suwon, Republic of Korea
[8]Department of Pharmacology, Yonsei University College of Medicine, Seoul, Republic of Korea
[9]Department of Psychiatry and Neuroscience, Icahn School of Medicine at Mount Sinai, New York, USA
[10]Department of Emerging Materials Science, DGIST, Daegu, Republic of Korea
[11]Brain Korea 21 Plus Project, Yonsei University College of Medicine, Seoul, Republic of Korea
[12]Severance Biomedical Science Institute, Yonsei University College of Medicine, Seoul, Republic of Korea
[13]Department of Chemistry, Yonsei University, Seoul, Republic of Korea
[14]Chan Zuckerberg Biohub, University of California San Francisco, CA, USA

*These authors contributed equally.
[†]Correspondence should be addressed to Z.J.G. (zev.gartner@ucsf.edu) or Y.J. (young-wook.jun@ucsf.edu).

Aberrant cleavage of Notch and amyloid precursor protein (APP) by γ-secretase is implicated in developmental disorders, cancer, and dementia. How cleavage is regulated in space and time is unclear. Here, we report that size-dependent protein segregation acts as a spatial switch regulating the dynamic distribution of these receptors relative to their enzymatic partner, γ-secretase. Because the size of the extracellular domain (ECD) greatly exceeds the width of the junctional cleft, Notch is excluded from cadherin-based adherens junctions (cadAJs) where γ-secretase localizes, prohibiting the enzyme-substrate interaction. ECD elimination by ADAM 10/17 drives a spatial rearrangement of Notch into cadAJs where γ-secretase cleavage occurs. Spatial mutation of Notch by decreasing (or increasing) the ECD size promotes (or inhibits) downstream signaling, respectively, regardless of ligand-presentation or S2 cleavage. Elimination of cadAJs abolishes Notch activation, confirming the indispensable role of cadAJs in regulating Notch-γ-secretase interactions. We further show that this spatial switch regulates APP cleavage and amyloid beta production. Therefore, size-dependent protein segregation creates membrane domains with unique proteolytic activities, choreographing the proteolytic sequence while suppressing nonspecific signal activation.

Notch is a highly conserved mediator for contact-dependent cell-cell communication, which orchestrates diverse functions in metazoans[1-5]. Tight control of Notch signal activation is essential for many developmental processes, while dysregulation of Notch activation can cause severe disease including developmental, neurological, and immunological disorders and cancer[1-8]. Accordingly, to enable precise signal regulation, receptor activation occurs through multiple steps, independently gated by chemical (e.g., ligand-receptor interactions, posttranslational modifications) and mechanical cues[4,5,9-27]. However, many signaling processes involving physical contact between two cells – so called juxtacrine signaling processes – are also regulated by spatial cues[28-31]. As exemplified by the kinetic segregation model in immune cells[28,32-43], spatial rearrangements of these signaling molecules modify their physical and biochemical environments to facilitate receptor activation. Notch, which also mediates signal exchange by physical contact, is subjected to similar structural and spatial rearrangements[44,45]. To test whether Notch signaling is regulated by these spatial rearrangements, we investigated the spatial dynamics of Notch and its signaling partners at cellular interfaces. Specifically, we focused on four key signaling molecules – Notch, delta-like ligand 1 (Dll1), ADAM 10, and γ-secretase, relative to cadherin-based adherens junctions (cadAJs); the cell-cell adhesions that initiate many structural and spatial changes by bringing and holding the membranes together[46-49] (**Fig. 1a**).

CadAJs segregate Notch from γ-secretase, preventing interactions

To map the distribution of Notch signaling components, we generated a series of U2OS cells expressing recombinant Notch1, Dll1, and/or epithelial cadherin (E-cadherin, Ecad) proteins. To facilitate the imaging of these proteins, we fused them with self-labeling tags (SNAP or Halo-tags) and/or fluorescent proteins (EGFP or mCherry) at the N- or C-termini, respectively (**Extended Data Table 1**). The endogenous Notch processing enzymes (*i.e.* ADAM 10, and γ-secretase) were immunostained and then imaged by confocal microscopy. With the exception of ADAM 10 which exhibited no preferential distribution relative to cadAJs (**Extended Data Fig. 1a**), all other proteins exhibited cadAJ-dependent localization (**Fig. 1b, c**). γ-secretase (visualized by staining with an anti-presenilin-1 antibody) was strongly enriched at the cadAJs with negligible non-junctional membrane signal (**Fig. 1b, c, Extended Data Fig. 1b, c**)[50]. In contrast, both Notch and Dll1 were excluded from cadAJs (**Fig. 1b, c**) and consequentially γ-secretase (**Extended Data Fig. 2a, b**). Notch exclusion from cadAJs was observed in multiple contexts, including different cadherin types, cell types, and cell polarization states (**Extended Data Fig. 3**). Quantitative analysis using the Manders' overlap coefficient to calculate fractional overlap with E-cadherin also confirmed the enrichment of γ-secretase (0.85 ± 0.21) at cadAJs and the exclusion of Notch (0.24 ± 0.19) and Dll1 (0.26 ± 0.18) from cadAJs (**Extended Data Fig. 2c, d**). These observations suggest two mechanisms by which cadAJs might influence Notch signaling: first, cadAJs recruit γ-secretase; second, cadAJs segregate Notch ligands and receptors from γ-secretase to prevent their interactions.

To interrogate how cadAJs drive the spatial segregation of the enzyme (*i.e.* γ-secretase) and substrate (*i.e.* Notch) pair, we employed our recently developed single-cell perturbation tool,

mechanogenetics, where magnetofluorescent nanoparticles (MFNs) control the location and mechanical loading of targeted receptors hence cell signaling[26,27,51]. Specifically, we clustered E-cadherin using mechanogenetics to generate artificial cadAJs that recapitulate the functional and signaling roles of native cadAJs[26,27,51] (**Fig. 1d, e**; See methods for more details). We then monitored the consequence of cadAJ formation on the spatial distributions of γ-secretase, Notch, and associated proteins (e.g. Flotillin-1, Flot1) relative to the artificial cadAJ (**Fig. 1f, g**). Consistent with the native cell-cell cadAJs, γ-secretase was localized at the artificial cadAJ (**Fig. 1f and Extended Data Fig. 4a, b**). We also observed colocalization of Flot1, a protein enriched in spatially discrete and ordered membrane microdomains at the artificial cadAJs[52-56] (**Fig. 1f and Extended Data Fig. 4a, b**). This observation, along with analysis of native cell-cell junctions (**Extended Data Fig. 4, c-g**), molecular dynamics (MD) simulation (**Extended Data Fig. 4, h-j**), and cholesterol depletion experiments (**Extended data Figs. 4k**), suggests that the cadAJs recruit and stabilize γ-secretase through a common spatially discrete and ordered membrane microdomains (for more discussion, see **Supplementary Discussion**).

Surprisingly, we observed an intense Notch signal at the artificial cadAJ (**Fig. 1g and Extended Data Fig. 5**), in contrast to the depleted Notch signal at native cell-cell cadAJs (**Fig. 1, a-c**). The extraordinarily large size (extended length = 136 nm[12], compacted height by electron microscopy > 20 nm[57]) of the Notch extracellular domain (NECD) suggested a potential explanation for these contradicting observations. Specifically, Notch could be excluded from cadAJs due to the NECD size greatly exceeding the narrow intermembrane cleft created by native cadAJs (20 nm)[47,58]. On the other hand, artificial cadAJs generated by MFNs are free of membrane juxtaposition and hence allow for Notch diffusion and accumulation, presumably through its association with γ-secretase or other components of the membrane microdomains[59]. These observations fit a model wherein the size-based physical constraint caused by cell-cell cadAJs segregates Notch from γ-secretase, preventing interactions that would otherwise serve to colocalize and concentrate the enzyme-substrate pair.

Size-dependent segregation choreographs the Notch proteolytic sequence

Upon activation by juxtacrine ligand-receptor interactions, Notch is processed by ADAM 10/17 (S2 cleavage) and then by γ-secretase (S3 cleavage), sequentially[1-5]. Since each of proteolytic events leads to a dramatic reduction in the size of NECD, we investigated how the size changes during activation correlate with its spatial distribution. We plated U2OS cells co-expressing SNAP-N^{FL}-mCherry and Ecad-GFP on a Dll4-coated substrate to trigger Notch activation. Cells were also treated with TAPI2 (an ADAM 10/17 inhibitor which stabilizes full-length Notch) or DAPT (a γ-secretase inhibitor that stabilizes the S2-cleaved Notch having a minimal extracellular domain) to capture Notch intermediates (**Fig. 2a**). To quantify the spatial redistribution of each Notch intermediate relative to the cadAJ, we measured the average mCherry fluorescence signal inside (I_{IN}) and outside (I_{OUT}) of the cadAJ and estimated an enrichment ratio (I_{IN}/I_{OUT}, See Methods). An intensity ratio of 1 represents no cadAJ-dependent distribution as validated with DiI dyes (I_{IN}/I_{OUT} = 1.07, **Fig. 2c and Extended Data 6a**), and values less

121 than or greater than 1 represent exclusion from or enrichment within cadAJs, respectively. With TAPI2,
122 we observed minimal mCherry fluorescence signal from cadAJs (I_{IN}/I_{OUT} = 0.50, **Fig. 2b**(ii)**, c**(ii)),
123 indicating that the ligand-receptor interaction did not alter the spatial distribution of Notch before S2
124 cleavage. In contrast, when TAPI2 was removed to activate S2 cleavage and DAPT was added to inhibit
125 S3 cleavage, we observed strong enrichment of the mCherry signal at cadAJs (I_{IN}/I_{OUT} = 2.14, **Fig. 2b**(iii)**,**
126 **c**(iii)), indicative of relocalization and concentration of the Notch extracellular domain truncation (NEXT),
127 the product of S2 cleavage, into cadAJs. When γ-secretase activity was rescued by washing out DAPT,
128 the initially intense mCherry signal at cadAJs gradually disappeared (**Fig. 2b**(iv)**, c**(iv)**, and Extended**
129 **Data Fig. 6b, c**), presumably corresponding to release of Notch intracellular domain (NICD) from the
130 membrane. These results suggest a role for the size-dependent protein segregation as a spatial switch
131 that regulates the distribution of Notch intermediates, thereby choreographing the sequential steps in
132 Notch proteolysis. According to this model, the mass of NECD poses a physical constraint preventing
133 entry of Notch to the narrow space between membranes in the cadAJ cleft where γ-secretase is localized.
134 Hence, γ-secretase cannot process the full-length Notch before S2 cleavage. Following S2 cleavage,
135 removal of NECD relieves the physical constraint, allowing Notch to enter into the cadAJ cleft. This
136 facilitates a productive Notch-γ-secretase interaction[59], S3 cleavage, and then downstream signaling.
137 To explore how size-dependent segregation controls Notch signaling, we first generated a series
138 of U2OS cell lines stably expressing Notch variants with different truncation lengths: a partial deletion of
139 the EGF repeats (NΔEGF$_{1\text{-}25}$, approximate height: 48 nm), complete deletion of the EGF repeats but
140 retention of negative regulatory region (NΔEGF, approximate height: 10 nm), and a complete removal of
141 NECD (NEXT, approximate height: 4 nm) (**Fig. 2d**). We fused these Notch variants with SNAP- and
142 mCherry-tags at their N- and C-termini, to differentially image the extracellular and intracellular domains.
143 All cells were treated with TAPI2 and DAPT to prevent any potential proteolysis of the variants. Consistent
144 with predictions based on size-dependent protein segregation, NΔEGF$_{1\text{-}25}$, the Notch variant with an ECD
145 taller than the height of the intermembrane cadAJ cleft, was excluded from cadAJs (I_{IN}/I_{OUT} = 0.57) (**Fig.**
146 **2e, f**). NEXT with an ECD smaller than the junctional height was enriched at cadAJs (I_{IN}/I_{OUT} = 2.39) (**Fig.**
147 **2e, f**). Interestingly, we observed binary localizations of NΔEGF (intermediate height) relative to cadAJs,
148 with a mean I_{IN}/I_{OUT} value of 1.32 (**Fig. 2e, f**). Some cadAJs displayed NΔEGF enrichment (**Fig. 2e**(bottom
149 left), **f**(right)), consistent with the size-based prediction. Meanwhile, other cadAJs excluded NΔEGF (**Fig.**
150 **2e**(bottom right)**, f**(right)). Considering the fact that cadherin cluster densities within cadAJs vary with the
151 size, type, and degree of junction maturation[60,61] and that the glycosylated negative regulatory region
152 domain[62] is susceptible to steric crowding, this unanticipated exclusion might result from a lateral
153 crowding effect in high-density cadAJs.
154 We then investigated the functional consequences of NΔEGF relocalization to cadAJs by
155 measuring the impact on downstream signaling process. Focusing on the subset of cadAJs showing
156 strong enrichment for Notch signal, we inferred γ-secretase activity by measuring the changes in
157 extracellular SNAP (labeled with SNAP surface dye) and intracellular mCherry fluorescence signals of

158 NΔEGF after DAPT removal while maintaining TAPI2 concentration. This construct has different
159 fluorescence markers on the extracellular and intracellular domains of the protein, allowing us to
160 differentially map the S2 and S3 cleavage events of the construct. While SNAP fluorescence signal
161 remained strong, the mCherry signal at the cadAJ was negligible (**Fig. 2g**). Similarly, colocalization
162 analysis of multiple cadAJs using Pearson correlation coefficients showed more significant signal
163 reduction in the mCherry channel than in SNAP, indicating selective release of NICD from cadAJs (**Fig.
164 2h**). We measured the kinetics of S3 processing by tracking mCherry intensity at the cadAJ in single cells.
165 Initially intense mCherry signals (average I_{IN}/I_{OUT} = 2.89 ± 1.15) rapidly dissipated within the first 2 hours
166 following DAPT removal (average I_{IN}/I_{OUT} = 0.81 ± 0.42), reaching a plateau at 4 hours (I_{IN}/I_{OUT} = 0.65 ±
167 0.14) **(Fig. 2i, j, and Extended Data Fig. 6d, e**). Removing DAPT did not elicit a significant reduction in
168 mCherry signal intensity from the non-cadAJ membrane, indicating that the S3 cleavage activity was
169 strongly localized at the cadAJ (**Extended Data Fig. 6f**). To confirm that the observed decrease in
170 mCherry signal at the cadAJ corresponds to the S3 cleavage, we performed western blot analysis of the
171 cells expressing the Notch variants. We cultured cells with TAPI2 to decouple γ-secretase processing
172 from S2 cleavage, and measured cleaved NICD levels by immunoblotting with Notch anti-V1744
173 antibodies. Cells expressing N^{FL} or $N\Delta EGF_{1-25}$ resulted in no or minimal NICD, respectively (**Fig. 2k, l**).
174 Whereas, cells expressing NΔEGF produced a significant amount of NICD (**Fig. 2k, l**). Cells expressing
175 NEXT exhibited the highest NICD production, about a 4-fold increase compared with that of NΔEGF (**Fig.
176 2k, l**). The observed NICD production levels were proportional to the enrichment ratio (I_{IN}/I_{OUT}) of the
177 Notch variants at cadAJs, suggesting the essential role of size-dependent protein segregation as a spatial
178 switch that controls Notch activation. Additionally, the substantial NICD production from the cells
179 expressing NΔEGF indicates that, when localized together, γ-secretase can process Notch, bypassing
180 S2 cleavage. Ligand-independent activation of Notch receptors with an intact S2 site was observed
181 previously in Notch truncation variants or synNotch constructs[63-65], but the mechanism of this activation
182 has been unclear so far. Our observations support the notion that colocalization of Notch with γ-secretase
183 is sufficient to trigger S3 proteolysis and signaling.

184 **Spatial mutation alters Notch signaling**

185 Prevailing models of Notch proteolysis by γ-secretase are based on the notion that S2-cleavage of Notch
186 serves to potentiate the cleavage by modifying the molecular interface at the enzyme-substrate pair[66,67].
187 For example, it has been suggested that γ-secretase selectively recognizes S2-cleaved Notch (*i.e.,* NEXT)
188 through hydrogen bonding between a glutamate residue in nicastrin and the new N-terminus of NEXT[66].
189 Another model proposed that S2 cleavage serves to reduce steric repulsion between nicastrin and NECD,
190 strengthening their interaction[67]. However, another key feature of S2 cleavage is that it generates a
191 smaller molecular intermediate that can uniquely access cadAJs, thereby colocalizing Notch with γ-
192 secretase and significantly increasing its concentration near the enzyme active site. This suggests a third

193 model, wherein γ-secretase activity on full length Notch and its intermediates is blocked by maintaining
194 Notch concentrations below the K_M for γ-secretase through spatial segregation.
195 To explicitly test the effect of Notch spatial localization relative to cadAJs and γ-secretase on the
196 signaling, we designed two experiments that induce spatial mutation of Notch. First, we employed a DNA-
197 mediated crosslinking strategy to enhance NΔEGF – a Notch variant that exhibited binary localizations
198 relative to cadAJs and relatively low Notch activation – enrichment at the cadAJ. We generated cells co-
199 expressing SNAP-NΔEGF-mCherry and Halo-Ecad-GFP, and treated the cells with complementary BG-
200 and chloroalkane-modified oligonucleotides in the presence of TAPI2 and DAPT (**Fig. 3a**). Notch-E-
201 cadherin heterodimers were formed efficiently as evidenced by the appearance of a higher molecular
202 weight band corresponding to the DNA-linked complex on western blots (**Extended Data Fig. 7a**).
203 Compared to untreated cells (I_{IN}/I_{OUT} = 1.32 ± 1.06), we observed further enrichment of NΔEGF at cadAJs
204 in the presence of DNA crosslinking (I_{IN}/I_{OUT} = 1.89 ± 0.91) (**Fig. 3b**). We then maintained cells in TAPI2
205 but removed DAPT to allow S3 cleavage. We observed decreases in mCherry signal at cadAJs after
206 DAPT removal, indicating efficient S3 cleavage without S2 cleavage (**Extended Data Fig. 7b-d**).
207 Interestingly, in western blots, we observed increased V1744-terminated NICD levels from the cells
208 treated with DNA crosslinkers, compared with the untreated control (**Fig. 3c**). There results suggest that
209 new molecular interfaces produced by mechanical activation and S2 cleavage are not necessary when
210 γ-secretase is concentrated with its substrate. Considering that DNA crosslinking (molecular weight =
211 21.4 kD) increases the ECD size of NΔEGF, the observed increase in NICD production cannot be
212 explained by the nicastrin-induced steric repulsion model. Hence, we concluded the result that increased
213 concentration of the NΔEGF at cadAJs facilitated its interaction with γ-secretase and promoted S3
214 cleavage.
215 To further test the importance of size-dependent spatial segregation, we induced spatial mutation
216 of NEXT (*i.e.* the Notch variant that showed the strongest enrichment at the cadAJ and activation) by
217 chemically conjugating it with macromolecules. Specifically, we conjugated BG-modified polymers and
218 proteins, to the extracellular SNAP tag (4.0 nm) of the variant via BG-SNAP chemistry (**Fig. 3d**). Grafting
219 of these macromolecular pendants onto NEXT increases the size of the Notch construct but does not
220 modify the N-terminal amine accessibility for hydrogen bonding with nicastrin. To interrogate the size-
221 dependent spatial mutation of NEXT systematically, we used a series of pendants with different
222 hydrodynamic sizes, that includes polyethylene glycol with an average molecular weight of 3.4 kD
223 (PEG3.4k, 2.5 nm), branched PEG20k (*b*PEG20k, 4.0 nm), linear PEG20k (ℓPEG20k, 8.0 nm), DNA-
224 streptavidin conjugates (DNA-stv, 9.5 nm), and human immunoglobulin G (hIgG, 12 nm) (**Fig. 3d and**
225 **Extended Data Fig. 8a**). In the presence of DAPT, we observed a size-dependent distribution of NEXT
226 at the cadAJ, where the larger pendant resulted in a greater decrease in mCherry signal at the cadAJ.
227 With pendants smaller than 5 nm (*i.e.* PEG3.4k and *b*PEG20*k*), NEXT remained enriched at the cadAJ
228 with I_{IN}/I_{OUT} of 2.21 and 2.01, respectively (**Fig. 3d, e**). When ℓPEG20k, DNA-stv, or hIgG were added,
229 we observed binary localizations of NEXT that were enriched at or excluded from the cadAJs, with mean

230 I_{IN}/I_{OUT} values of 1.06, 0.82, 0.98, respectively (**Fig. 3d, e**). These observations were similar to the spatial
231 behaviors of NΔEGF having a comparable ECD size, where only less dense cadAJs allowed Notch
232 colocalization. We then examined the signaling consequences of each size-dependent spatial mutation
233 of NEXT. Following S3 cleavage, NICD traffics to the nucleus, allowing us to measure nuclear mCherry
234 signal as a proxy for Notch pathway activation. The PEG3.4k or *b*PEG20k addition did not significantly
235 alter nuclear mCherry signal of NEXT, compared with cells with no pendant addition (**Fig. 3f, g and**
236 **Extended Fig. 9b**). Conjugation of ℓPEG20k, DNA-stv (9.5 nm) resulted in substantial decrease in
237 nuclear mCherry signal to 0.39 and 0.37, respectively (**Fig. 3f, g and Extended Fig. 8b**). hIgG addition
238 slightly further suppressed nuclear mCherry signal to 0.27 (**Fig. 3f, g and Extended Fig. 8b**). Finally, we
239 summarized the S3-cleaved NICD production of all Notch variants as a function of the Notch enrichment
240 factor, I_{IN}/I_{OUT}, in **Fig. 3h**, clearly visualizing the spatial dependence of S3 cleavage.

241 **The cadAJ-mediated spatial switch is indispensable for Notch signaling**

242 Given the significant role of cadAJs in coordinating the spatial dynamics of Notch and γ-secretase, we
243 next interrogated Notch signal activation in cells lacking cadAJs. To minimize physical contact between
244 cells and hence cadAJ formation, we sparsely plated cells expressing SNAP-Notch-Gal4 (SNAP-N^{FL}-
245 Gal4) receptors on a Dll4-coated substrate. We used a UAS-Gal4 reporter system that detects Notch
246 activation with nuclear mCherry signal[15,23,26]. After 16 hours from cell seeding, we measured the mCherry
247 fluorescence in cells having no prior contact with other cells. For comparison, we also analyzed the
248 mCherry signal in cells with robust cadAJs within high-density culture. While the cells with physical
249 contacts with other cells exhibited robust increase in nuclear mCherry fluorescence signal, those without
250 cell-cell contact elicited no increase in signal (**Fig. 4a, b and Supplementary Video 1**). Reestablishing
251 the cadAJs by plating cells on a substrate coated with Ecad-Fc and Dll4-Fc rescued the Notch signaling
252 of the solitary cells (**Fig. 4a, c, and Supplementary Video 2**). These results support that cadAJs are
253 required for Notch processing at the cell surface and downstream signaling. Critically, E-cadherin seems
254 to function in this capacity in a manner that is independent of its role in mediating cell-cell contact. To
255 further test this notion, we knocked out the gene encoding E-cadherin (CDH1) in the reporter cell line via
256 CRISPR-Cas9, then plated the cells at high density on Dll4-Fc coated plates (**Extended Data Fig 9**, **a-**
257 **f**). Strikingly, E-cadherin knockout (Ecad-KO) resulted in abrogation of Notch activation even with robust
258 cell-cell contact (**Fig. 4d**, **e, and Extended Data Fig. 9g**). Reintroduction of plasmids encoding E-
259 cadherin or N-cadherin into Ecad-KO cells recovered Notch activation with substantial nuclear mCherry
260 signal, confirming the indispensable role of cadAJs in Notch signaling (**Fig. 4d, e and Extended Data**
261 **Fig. 9g**).

262 **Size-dependent spatial dynamics and proteolysis of amyloid precursor proteins**

263 The proteolysis processes of amyloid precursor protein (APP) plays a central role in amyloid beta (Aβ)
264 pathology, which can cause failures in many organs such as brain, heart, kidney, and vasculatures[68-71].
265 Interestingly, APP has a strikingly similar topology and proteolytic cleavage sequence to that of Notch.

266 APP possesses a large ECD (> 20 nm) and is processed by α- or β-secretase and then γ-secretase[68-71].
267 These characteristics motivated us to investigate the role of the size-dependent protein segregation in
268 APP processing. We generated U2OS cells co-expressing APP-GFP and SNAP-N-cadherin (SNAP-
269 Ncad) and monitored the cell surface spatial dynamics of APP intermediates relative to N-cadherin based
270 AJs (NcadAJs) using proteolytic enzyme inhibitors. Similar to Notch, we found that APP was initially
271 excluded from NcadAJs, diffused into the NcadAJs after the ECD shedding by α- or β-secretase, and
272 then was processed by γ-secretase within it (**Fig. 4f**).

273 APP can be processed along two pathways by γ-secretase – one pathway occurs at the cell
274 surface to generate more soluble isoforms including p3 or $A\beta_{40}$, the other pathway occurs internally to
275 produce less soluble and pathogenic $A\beta_{42}$[68-73]. Given our previous observation that loss of cadAJs leads
276 to a decrease in cell surface γ-secretase, we hypothesized that APP processing would be biased under
277 these conditions towards $A\beta_{42}$. We tested this hypothesis by constructing U2OS cell lines lacking both E-
278 and N-cadherins (cad-KO cells) using CRISPR-Cas9 (**Extended Data Fig. 9h, i**). We then transfected
279 plain U2OS cells or cad-KO cells with a plasmid encoding APP sequence and measured Aβ production
280 by ELISA. Consistent with the hypothesis, cad-KO cells produced higher $A\beta_{42}$, the isoform prone to
281 severe fibril aggregation, compared to cells with endogenous cadherin expression (**Fig. 4g**).

282 **Discussion**

283 Notch displays several unique features that are distinct from other juxtacrine receptors. For example,
284 unlike classical receptor signaling, the Notch ligand-receptor interaction (chemical switch) is converted
285 into intracellular signaling through a sequence of additional signaling switches acting by mechanical,
286 enzymatic, and spatial mechanisms. These include unfolding of the negative regulatory region domain
287 (mechanical switch), S2- and S3- cleavages (enzymatic switch), and finally translocation of the NICD
288 from the cell membrane to the nucleus (spatial switch)[4,5]. Our study reveals that Notch additionally
289 integrates a spatial switch at the cell surface to tightly choreograph the enzymatic cleavage sequence
290 prior to NICD release. Previously, it was thought that this enzymatic sequence was regulated by
291 modification of the molecular interface between Notch and nicastrin after S2-cleavage[66,67]. Our model
292 does not rule out the contribution of the nicastrin-Notch chemical interface during this process, but our
293 study strongly suggests that the spatial switch is the major regulator of Notch-γ-secretase interaction and
294 signaling, functioning by increasing the concentration of the γ-secretase substrate to the point that it is
295 efficiently processed by the enzyme. Particularly, our mechanogenetic and the NΔEGF cleavage
296 experiment shown in Figure 1(d-g) and 2(e-l), respectively, support the notion that Notch with an intact
297 S2 site is effectively engaged and then processed by γ-secretase when the spatial constraints are
298 removed.

299 The operating principle of the spatial switch is closely related to another unique feature of Notch
300 receptor: the unusually tall NECD. The functional residues responsible for ligand binding are located near
301 the N-terminus, which protrudes above the crowded cell surface, where they are poised to engage ligands

302 on neighboring cells. Surprisingly, however, it has been also shown that replacing the EGF-like domain
303 repeats with a relatively smaller ligand binding domain (e.g. synNotch) maintains the receptor function[74,75].
304 Why then does Notch receptor bear such a massive ECD? Our study provides insight into this question,
305 where the large ECD is crucial for its spatial segregation from γ-secretase thereby minimizing nonspecific
306 ligand-independent activation. Low level NICD production was observed even for the Notch variants with
307 a partial EGF truncation ($N\Delta EGF_{1-25}$), and levels gradually increased upon successive truncations to the
308 NECD size. Our model also explains previous observations where synNotch with a relatively small ECD
309 exhibited significant ligand-independent activation (10-50% of ligand-induced activation)[64].

310 We also show that the size-dependent spatial segregation regulates APP cleavage and Aβ
311 production. It has been previously shown that γ-secretase presenting in different subcellular
312 compartments cleaves APP into diverse Aβ isoforms[70,73,76-78]. Our study shows that, after the ECD
313 cleavage, cadAJ potentiates cell surface processing of APPs within the junction, yielding $A\beta_{40}$
314 predominantly, while removal of cadAJ produces more $A\beta_{42}$. To establish the relevance of this
315 observation to APP processing will require further investigation in a neuronal system, but our results in
316 model cell lines are consistent with the predominant secretion of Aβ from synapse, where N-cadherin
317 junctions localize[79,80].

318 The spatial switch is analogous to the kinetic segregation model of T cell activation, where large
319 CD45 phosphatase is excluded from T cell receptor (TCR) immunological synaptic clefts[28,32-42]. However,
320 there are several distinct features of the Notch spatial switch compared to the kinetic segregation model.
321 First, unlike the immunological synapse where TCR and CD45 remain constant in size throughout
322 activation, Notch undergoes a dramatic size change during the course of cell surface activation, enabling
323 its dynamic spatial redistribution and sequential proteolysis. Second, the role of cadAJs in Notch signaling
324 is not limited to creating a physical barrier, but also plays the critical role of recruiting γ-secretase to
325 facilitate processing of S2-cleaved Notch at the cell surface. Third and finally, the consequences of size-
326 dependent segregation on signaling are reversed compared to the immunological synapse. While spatial
327 segregation of CD45 enables sustained TCR phosphorylation and downstream signaling, Notch
328 segregation from cadAJs inhibits signal activation. Our result extends the relevance of size-dependent
329 spatial segregation models beyond immune cells, [28,32-43], supporting the notion that the size-dependent
330 protein segregation can serve as a general mechanism for regulating a broad range of receptor signaling
331 at the cell-cell interface, including Notch and APPs.

332 Overall, a spatial switching mechanism based on size-dependent protein segregation not only
333 sheds light on the mechanism underlying the sequential proteolysis of Notch and APPs, but also may
334 extend to other receptors processed by γ-secretase. Finally, we anticipate further implications of our work
335 in other areas of research such as providing new design principles for synthetic receptors like synNotch,
336 as well as new therapeutic approaches that target Notch and APP signaling by spatial mutation in cancer
337 and neurodegenerative diseases.

338 1. Artavanis-Tsakonas, S., Rand, M. D. & Lake, R. J. Notch Signaling: Cell Fate Control and Signal
339 Integration in Development. *Science* **284,** 770–776 (1999).
340 2. Fortini, M. E. Notch signaling: the core pathway and its posttranslational regulation. *Dev. Cell* **16,**
341 633–647 (2009).
342 3. Louvi, A. & Artavanis-Tsakonas, S. Notch signalling in vertebrate neural development. *Nat. Rev.*
343 *Neurosci.* **7,** 93–102 (2006).
344 4. Bray, S. J. Notch signalling in context. *Nat. Rev. Mol. Cell Biol.* **17,** 722–735 (2016).
345 5. Kovall, R. A., Gebelein, B., Sprinzak, D. & Kopan, R. The Canonical Notch Signaling Pathway:
346 Structural and Biochemical Insights into Shape, Sugar, and Force. *Dev. Cell* **41,** 228–241 (2017).
347 6. Koch, U. & Radtke, F. Notch and cancer: a double-edged sword. *Cell. Mol. Life Sci.* **64,** 2746–
348 2762 (2007).
349 7. South, A. P., Cho, R. J. & Aster, J. C. The double-edged sword of Notch signaling in cancer.
350 *Semin. Cell Dev. Biol.* **23,** 458–464 (2012).
351 8. Lai, E. C. Notch signaling: control of cell communication and cell fate. *Development* **131,** 965–
352 973 (2004).
353 9. Luca, V. C. *et al.* Notch-Jagged complex structure implicates a catch bond in tuning ligand
354 sensitivity. *Science* **355,** 1320–1324 (2017).
355 10. Haines, N. & Irvine, K. D. Glycosylation regulates Notch signalling. *Nat. Rev. Mol. Cell Biol.* **4,**
356 786–797 (2003).
357 11. D'Souza, B., Miyamoto, A. & Weinmaster, G. The many facets of Notch ligands. *Oncogene* **27,**
358 5148–5167 (2008).
359 12. Luca, V. C. *et al.* Structural biology. Structural basis for Notch1 engagement of Delta-like 4.
360 *Science* **347,** 847–853 (2015).
361 13. Moloney, D. J. *et al.* Fringe is a glycosyltransferase that modifies Notch. *Nature* **406,** 369–375
362 (2000).
363 14. Brückner, K., Perez, L., Clausen, H. & Cohen, S. Glycosyltransferase activity of Fringe
364 modulates Notch-Delta interactions. *Nature* **406,** 411–415 (2000).
365 15. Sprinzak, D. *et al.* Cis-interactions between Notch and Delta generate mutually exclusive
366 signalling states. *Nature* **465,** 86–90 (2010).
367 16. Nandagopal, N. *et al.* Dynamic Ligand Discrimination in the Notch Signaling Pathway. *Cell* **172,**
368 869–880.e19 (2018).
369 17. Lebon, L., Lee, T. V., Sprinzak, D., Jafar-Nejad, H. & Elowitz, M. B. Fringe proteins modulate
370 Notch-ligand cis and trans interactions to specify signaling states. *Elife* **3,** e02950 (2014).
371 18. Shaya, O. *et al.* Cell-Cell Contact Area Affects Notch Signaling and Notch-Dependent Patterning.
372 *Dev. Cell* **40,** 505–511.e6 (2017).
373 19. Weinmaster, G. & Fischer, J. A. Notch Ligand Ubiquitylation: What Is It Good For? *Dev. Cell* **21,**
374 134–144 (2011).

375 20. Baron, M. *et al.* Multiple levels of Notch signal regulation. *Mol. Membr. Biol.* **19,** 27–38 (2002).
376 21. Yamamoto, S. *et al.* A mutation in EGF repeat-8 of Notch discriminates between Serrate/Jagged
377 and Delta family ligands. *Science* **338,** 1229–1232 (2012).
378 22. Wang, X. & Ha, T. Defining single molecular forces required to activate integrin and notch
379 signaling. *Science* **340,** 991–994 (2013).
380 23. Gordon, W. R. *et al.* Mechanical Allostery: Evidence for a Force Requirement in the Proteolytic
381 Activation of Notch. *Dev. Cell* **33,** 729–736 (2015).
382 24. Meloty-Kapella, L., Shergill, B., Kuon, J., Botvinick, E. & Weinmaster, G. Notch ligand
383 endocytosis generates mechanical pulling force dependent on dynamin, epsins, and actin. *Dev.*
384 *Cell* **22,** 1299–1312 (2012).
385 25. Shergill, B., Meloty-Kapella, L., Musse, A. A., Weinmaster, G. & Botvinick, E. Optical tweezers
386 studies on Notch: single-molecule interaction strength is independent of ligand endocytosis. *Dev.*
387 *Cell* **22,** 1313–1320 (2012).
388 26. Seo, D. *et al.* A Mechanogenetic Toolkit for Interrogating Cell Signaling in Space and Time. *Cell*
389 **165,** 1507–1518 (2016).
390 27. Kim, J.-W. *et al.* Single-cell mechanogenetics using monovalent magnetoplasmonic
391 nanoparticles. *Nat. Protoc.* **12,** 1871–1889 (2017).
392 28. Bell, G. I. Models for the specific adhesion of cells to cells. *Science* **200,** 618–627 (1978).
393 29. Manz, B. N. & Groves, J. T. Spatial organization and signal transduction at intercellular junctions.
394 *Nat. Rev. Mol. Cell Biol.* **11,** 342–352 (2010).
395 30. Schmid, E. M. *et al.* Size-dependent protein segregation at membrane interfaces. *Nat. Phys.* **12,**
396 704–711 (2016).
397 31. Salaita, K. *et al.* Restriction of receptor movement alters cellular response: physical force
398 sensing by EphA2. *Science* **327,** 1380–1385 (2010).
399 32. Dustin, M. L. & Shaw, A. S. Costimulation: Building an Immunological Synapse. *Science* **283,**
400 649–650 (1999).
401 33. Aricescu, A. R. *et al.* Structure of a tyrosine phosphatase adhesive interaction reveals a spacer-
402 clamp mechanism. *Science* **317,** 1217–1220 (2007).
403 34. Monks, C. R., Freiberg, B. A., Kupfer, H., Sciaky, N. & Kupfer, A. Three-dimensional segregation
404 of supramolecular activation clusters in T cells. *Nature* **395,** 82–86 (1998).
405 35. Dustin, M. L. Making a little affinity go a long way: a topological view of LFA-1 regulation. *Cell*
406 *Adhes. Commun.* **6,** 255–262 (1998).
407 36. Grakoui, A. *et al.* The immunological synapse: a molecular machine controlling T cell activation.
408 *Science* **285,** 221–227 (1999).
409 37. James, J. R. & Vale, R. D. Biophysical mechanism of T-cell receptor triggering in a reconstituted
410 system. *Nature* **487,** 64–69 (2012).

411 38. Cordoba, S.-P. *et al.* The large ectodomains of CD45 and CD148 regulate their segregation from
412 and inhibition of ligated T-cell receptor. *Blood* **121,** 4295–4302 (2013).
413 39. Dustin, M. L. & Groves, J. T. Receptor signaling clusters in the immune synapse. *Annu. Rev.*
414 *Biophys.* **41,** 543–556 (2012).
415 40. Wülfing, C. & Davis, M. M. A receptor/cytoskeletal movement triggered by costimulation during T
416 cell activation. *Science* **282,** 2266–2269 (1998).
417 41. Choudhuri, K., Wiseman, D., Brown, M. H., Gould, K. & van der Merwe, P. A. T-cell receptor
418 triggering is critically dependent on the dimensions of its peptide-MHC ligand. *Nature* **436,** 578–
419 582 (2005).
420 42. Groves, J. T. & Kuriyan, J. Molecular mechanisms in signal transduction at the membrane. *Nat.*
421 *Struct. Mol. Biol.* **17,** 659–665 (2010).
422 43. Bakalar, M. H. *et al.* Size-Dependent Segregation Controls Macrophage Phagocytosis of
423 Antibody-Opsonized Targets. *Cell* **174,** 131–142.e13 (2018).
424 44. Luty, W. H., Rodeberg, D., Parness, J. & Vyas, Y. M. Antiparallel segregation of notch
425 components in the immunological synapse directs reciprocal signaling in allogeneic Th: DC
426 conjugates. *The Journal of Immunology* **179,** 819–829 (2007).
427 45. Narui, Y. & Salaita, K. Membrane tethered delta activates notch and reveals a role for spatio-
428 mechanical regulation of the signaling pathway. *Biophys. J.* **105,** 2655–2665 (2013).
429 46. Yap, A. S. & Kovacs, E. M. Direct cadherin-activated cell signaling: a view from the plasma
430 membrane. *J. Cell Biol.* **160,** 11–16 (2003).
431 47. Harrison, O. J. *et al.* The extracellular architecture of adherens junctions revealed by crystal
432 structures of type I cadherins. *Structure* **19,** 244–256 (2011).
433 48. Adams, C. L., Chen, Y. T., Smith, S. J. & Nelson, W. J. Mechanisms of epithelial cell-cell
434 adhesion and cell compaction revealed by high-resolution tracking of E-cadherin-green
435 fluorescent protein. *J. Cell Biol.* **142,** 1105–1119 (1998).
436 49. Chen, C. S., Tan, J. & Tien, J. Mechanotransduction at cell-matrix and cell-cell contacts. *Annu.*
437 *Rev. Biomed. Eng.* **6,** 275–302 (2004).
438 50. Kouchi, Z. *et al.* p120 catenin recruits cadherins to gamma-secretase and inhibits production of
439 Abeta peptide. *J. Biol. Chem.* **284,** 1954–1961 (2009).
440 51. Kwak, M. *et al.* Small, Clickable, and Monovalent Magnetofluorescent Nanoparticles Enable
441 Mechanogenetic Regulation of Receptors in a Crowded Live-Cell Microenvironment. *Nano Lett.*
442 **19,** 3761–3769 (2019).
443 52. Causeret, M., Taulet, N., Comunale, F., Favard, C. & Gauthier-Rouvière, C. N-cadherin
444 association with lipid rafts regulates its dynamic assembly at cell-cell junctions in C2C12
445 myoblasts. *Mol. Biol. Cell* **16,** 2168–2180 (2005).

446 53. Taulet, N. *et al.* N-cadherin/p120 catenin association at cell-cell contacts occurs in cholesterol-
447 rich membrane domains and is required for RhoA activation and myogenesis. *J. Biol. Chem.*
448 **284,** 23137–23145 (2009).
449 54. Yap, A. S., Gomez, G. A. & Parton, R. G. Adherens Junctions Revisualized: Organizing
450 Cadherins as Nanoassemblies. *Dev. Cell* **35,** 12–20 (2015).
451 55. Guillaume, E. *et al.* Flotillin microdomains stabilize cadherins at cell-cell junctions. *J. Cell. Sci.*
452 **126,** 5293–5304 (2013).
453 56. Vetrivel, K. S. *et al.* Spatial segregation of gamma-secretase and substrates in distinct
454 membrane domains. *J. Biol. Chem.* **280,** 25892–25900 (2005).
455 57. Kelly, D. F. *et al.* Molecular structure and dimeric organization of the Notch extracellular domain
456 as revealed by electron microscopy. *PLoS ONE* **5,** e10532 (2010).
457 58. Brasch, J., Harrison, O. J., Honig, B. & Shapiro, L. Thinking outside the cell: how cadherins drive
458 adhesion. *Trends Cell Biol.* **22,** 299–310 (2012).
459 59. Polacheck, W. J. *et al.* A non-canonical Notch complex regulates adherens junctions and
460 vascular barrier function. *Nature* **552,** 258–262 (2017).
461 60. Indra, I. *et al.* Spatial and temporal organization of cadherin in punctate adherens junctions.
462 *Proc. Natl. Acad. Sci. U.S.A.* **115,** E4406–E4415 (2018).
463 61. Takeichi, M. Dynamic contacts: rearranging adherens junctions to drive epithelial remodelling.
464 *Nat. Rev. Mol. Cell Biol.* **15,** 397–410 (2014).
465 62. Takeuchi, H. & Haltiwanger, R. S. Role of glycosylation of Notch in development. *Semin. Cell*
466 *Dev. Biol.* **21,** 638–645 (2010).
467 63. Palmer, W. H. & Deng, W.-M. Ligand-Independent Mechanisms of Notch Activity. *Trends Cell*
468 *Biol.* **25,** 697–707 (2015).
469 64. Yang, Z.-J., Yu, Z.-Y., Cai, Y.-M., Du, R.-R. & Cai, L. Engineering of an enhanced synthetic
470 Notch receptor by reducing ligand-independent activation. *Commun. Biol.* **3,** 116 (2020).
471 65. Mumm, J. S. *et al.* A ligand-induced extracellular cleavage regulates gamma-secretase-like
472 proteolytic activation of Notch1. *Mol. Cell* **5,** 197–206 (2000).
473 66. Shah, S. *et al.* Nicastrin functions as a gamma-secretase-substrate receptor. *Cell* **122,** 435–447
474 (2005).
475 67. Bolduc, D. M., Montagna, D. R., Gu, Y., Selkoe, D. J. & Wolfe, M. S. Nicastrin functions to
476 sterically hinder γ-secretase-substrate interactions driven by substrate transmembrane domain.
477 *Proc. Natl. Acad. Sci. U.S.A.* **113,** E509–18 (2016).
478 68. Sala Frigerio, C. & De Strooper, B. Alzheimer's Disease Mechanisms and Emerging Roads to
479 Novel Therapeutics. *Annu. Rev. Neurosci.* **39,** 57–79 (2016).
480 69. O'Brien, R. J. & Wong, P. C. Amyloid precursor protein processing and Alzheimer's disease.
481 *Annu. Rev. Neurosci.* **34,** 185–204 (2011).

482 70. Selkoe, D. J. & Hardy, J. The amyloid hypothesis of Alzheimer's disease at 25 years. *EMBO Mol.*
483 *Med.* **8,** 595–608 (2016).
484 71. Pepys, M. B. Amyloidosis. *Annu. Rev. Med.* **57,** 223–241 (2006).
485 72. Ehehalt, R., Keller, P., Haass, C., Thiele, C. & Simons, K. Amyloidogenic processing of the
486 Alzheimer beta-amyloid precursor protein depends on lipid rafts. *J. Cell Biol.* **160,** 113–123
487 (2003).
488 73. De Strooper, B. & Karran, E. The Cellular Phase of Alzheimer's Disease. *Cell* **164,** 603–615
489 (2016).
490 74. Morsut, L. *et al.* Engineering Customized Cell Sensing and Response Behaviors Using Synthetic
491 Notch Receptors. *Cell* **164,** 780–791 (2016).
492 75. Engineering T Cells with Customized Therapeutic Response Programs Using Synthetic Notch
493 Receptors. *Cell* **167,** 419–432.e16 (2016).
494 76. Chow, V. W., Mattson, M. P., Wong, P. C. & Gleichmann, M. An overview of APP processing
495 enzymes and products. *Neuromolecular Med.* **12,** 1–12 (2010).
496 77. Yang, G. *et al.* Structural basis of Notch recognition by human γ-secretase. *Nature* **565,** 192–197
497 (2019).
498 78. Bolduc, D. M., Montagna, D. R., Seghers, M. C., Wolfe, M. S. & Selkoe, D. J. The amyloid-beta
499 forming tripeptide cleavage mechanism of γ-secretase. *Elife* **5,** 08928 (2016).
500 79. Yuksel, M. & Tacal, O. Trafficking and proteolytic processing of amyloid precursor protein and
501 secretases in Alzheimer's disease development: An up-to-date review. *Eur. J. Pharmacol.* **856,**
502 172415 (2019).
503 80. Arikkath, J. N-cadherin: stabilizing synapses. *J. Cell Biol.* **189,** 397–398 (2010).
504
505

506 **Acknowledgement**
507 The authors thank Drs. Stephen Blacklow (Harvard U.) and C. Miller (King's College London) for the kind
508 gifts of Notch and APP plasmids, respectively. We also thank Dr. Daniel Fletcher (UC Berkeley), Mr. Ari
509 Joffe (UC Berkeley), and Dr. Duaa Al-Rawi (Stanford U.) for helpful discussion. For reagents, technical
510 supports, and discussions we thank the Kim, Cheon, Gartner, and Jun laboratories, as well as the Nikon
511 Imaging Center and Wynton at UCSF. M.K. was supported by a Life Science Research Foundation
512 fellowship as the Shurl and Kay Curci Foundation fellow, and by Burroughs Wellcome Travel Fund. This
513 work was supported by 2020R1A2C4002533 (D.S.) and NRF-2017R1A2B3004198 (H.K.), HI17C0676
514 from Korean Ministry of Health and Welfare (H.K.), 5R01AG008200 from National Institute on Aging (NIA)
515 and the National Institute of Health (NIH) (N.K.R.), IBS-R026-D1 from IBS (H.K. and J.C.), NRF-
516 2019R1A2C1085712 (Y.H.K.), the UCSF Center for Cellular Construction (an NSF Science and
517 Technology Center, no. DBI-1548297) (Z.J.G.), U01CA244109 from the National Cancer Institute (Z.J.G),
518 1R01GM112081, 1R01GM126542-01, and R35GM134948 from the National Institute of General Medical
519 Science (NIGMS) and the NIH (Y.J.), and the UCSF Program for Breakthrough Biomedical Research
520 (PBBR) funded in part by the Sandler Foundation (Y.J.). Z.J.G. is a Chan Zuckerberg BioHub Investigator.

521 **Author contributions**
522 M.K., K.M.S., Z.J.G., and Y.J. conceived the ideas and designed research; M.K. and K.M.S. constructed
523 plasmids, generated cell lines, and performed confocal microscopy. M.K. performed mechanogenetics,
524 truncation study, spatial mutation, immunoblot analysis, reporter cell assay, and APP experiment. K.M.S.
525 performed Notch exclusion and activation experiments, designed truncation study, wrote custom python
526 image analysis scripts. N.K. performed coarse-grained MD simulation. R.G. generated cadherin-KO cells.
527 W.R.K. performed flotillin staining and mechanogenetic experiment. M.A. and H.L. synthesized magnetic
528 nanoparticles and helped confocal imaging. J.F. and D.S. performed initial proof-of-concept experiment.
529 A.G. and N.K.R. provided anti-PS1 antibodies. H.K., Y.H.K., and J.C. oversaw and supervised CRISPR-
530 Cas9 KO experiment, MD simulation, and magnetic nanoparticle synthesis, respectively. Z.J.G. oversaw
531 and supervised all spatial mapping and mutation experiments. Y.J. oversaw and supervised all aspects
532 of the experiment. M.K. and K.M.S. analyzed data. M.K., K.M.S., Z.J.G., and Y.J. wrote the manuscript.

533 **Competing interests**
534 The authors declare no competing interest.

535 **Additional information**

536 **Supplementary Information** is available for this paper.
537

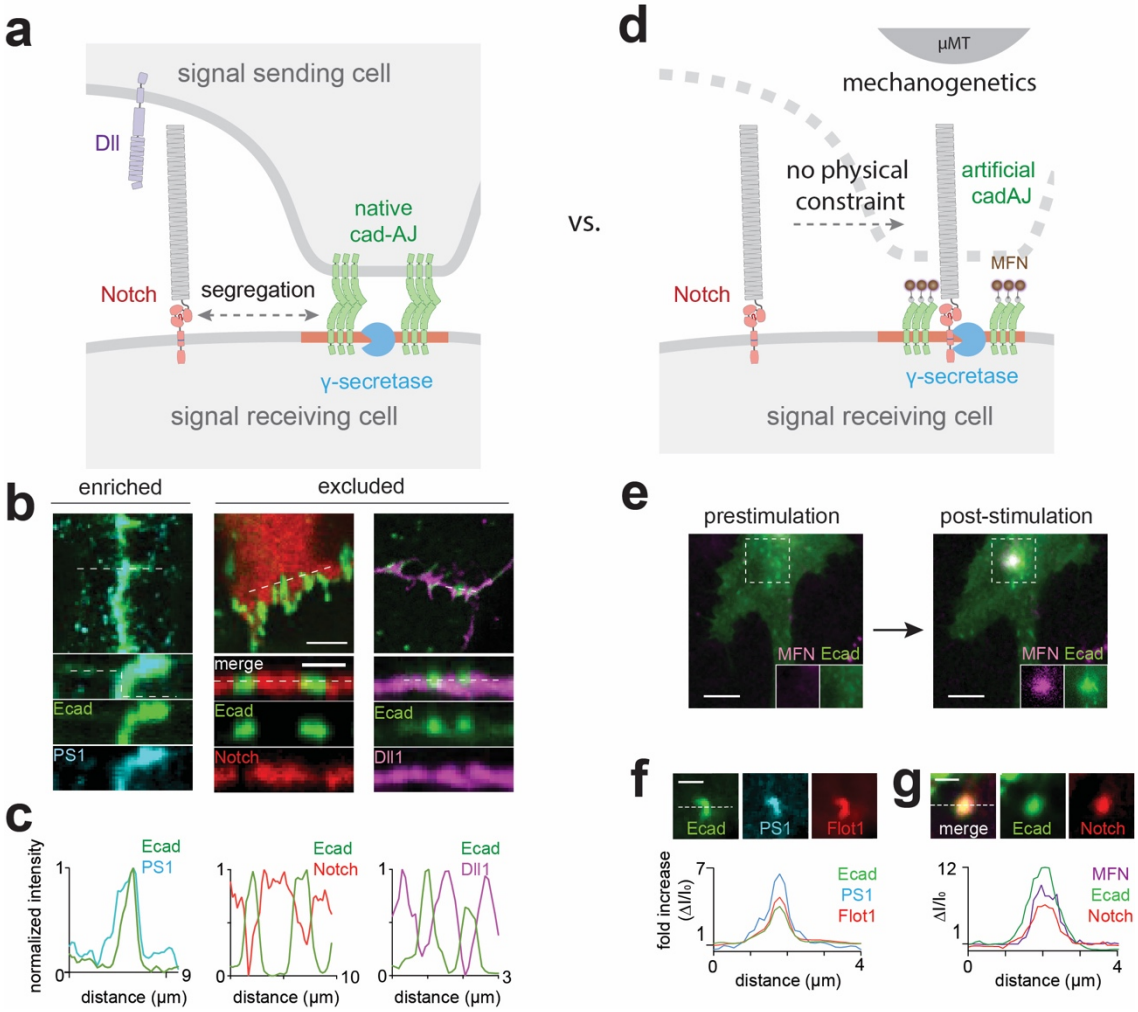

Figure 1. Spatial segregation of Notch receptors and ligands from cadAJs prevents their interactions with γ-secretase. a, A schematic showing spatial distribution of Notch signaling components at the juxtaposed cell-cell interface. **b,** Representative confocal fluorescence images showing presenilin-1 (PS1), Notch1, and Dll1 distributions relative to E-cadherin-based cadherin junction (cadAJ). (top) A maximum projection image. Scale bar, 5 μm. (bottom) z-resliced images. Scale bar, 3 μm. PS1 was strongly enriched at the cadAJ, whereas Notch1 and Dll1 were segregated from the cadAJ. **c,** Line profiles quantifying fluorescence from E-cadherin (green), PS1 (cyan), Notch (red), and Dll1 (magenta) along a representative section of the cadAJ (a white dashed line in panel **b**, z-resliced images). **d,** A schematic showing mechanogenetic interrogation of γ-secretase and Notch distribution relative to the artificial cadAJs. Artificial cadAJs were formed by clustering Ecad-GFP labeled with magnetofluorescent nanoparticles (MFNs) by application of an external micromagnetic tweezer (μMT). DAPT was used to inhibit γ-secretase activity during mechanogenetic interrogation of Notch/γ-secretase interaction in absence of the membrane juxtaposition. **e,** Epifluorescence images showing the formation of an artificial cadAJ by mechanogenetics. After stimulation by μMT, vivid MFN and E-cadherin signals at the magnetic focus were seen, indicating formation of cadAJs. Scale bar, 5 μm. **f,** Confocal fluorescence images of E-cadherin, PS1, and Flotillin-1 (Flot1) at the artificial cadAJ. Scale bar, 2 μm. Line profiles of E-cadherin, PS1 and Flot1 signals along a white dashed line. $\Delta I/I_0$ represents a fold change relative to nonjunctional membrane signals. **g,** Confocal fluorescence images showing E-cadherin and Notch distributions at the artificial cadAJs after μMT application. Strong accumulation of Notch signals at the artificial cadAJ was clearly seen. Line profiles of MFN, E-cadherin, and Notch signals along a white dashed line. $\Delta I/I_0$ represents a fold change relative to fluorescence intensity before stimulation. Scale bar, 2 μm.

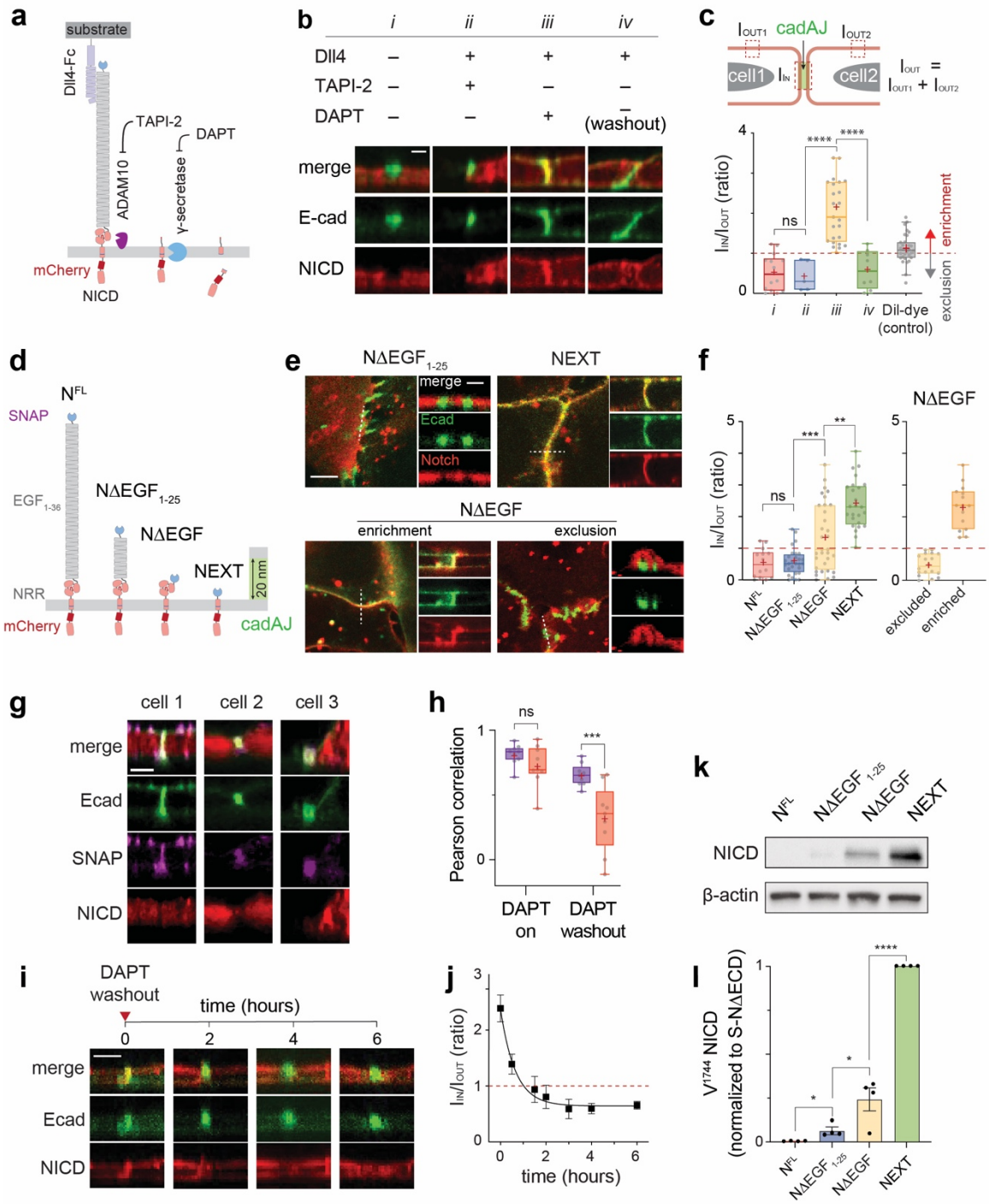

Figure 2. Size-dependent segregation of Notch at the cadAJs controls the proteolytic sequence. **a,** A schematic to capture the spatial distribution of Notch intermediates during the cell-surface activation pathway. **b,** Confocal z-resliced images showing Notch distribution (red) relative to cadAJ (green) from the cells without Dll4 activation (i), treated with Dll4 and TAPI2 (ii), treated with Dll4 and DAPT (iii), and washed out to remove DAPT inhibition (iv). Scale bar, 3 μm. **c,** Quantification of Notch signal enrichment at the cadAJs during the activation. Notch enrichment (I_{IN}/I_{OUT}) is calculated as the ratio of average Notch fluorescence intensity within cadAJs (I_{IN}) and outside cadAJ (I_{OUT}). The enrichment factor of Dil is present as a control showing cadAJ-independent distribution. ****P < 0.0001, ns: non-significant, one-way ordinary ANOVA followed by Tukey's multiple comparison testing. **d,** Schematics of Notch variants with different truncation lengths, in comparison with the cadAJ intermembrane cleft. **e,** Confocal fluorescence images showing spatial distribution of the Notch variants (red) relative to the cadAJs (green). To prevent any ligand-independent activation, cells were incubated with TAPI-2 and DAPT. (left) Maximum

projections of confocal z-stacks are shown. Scale bar, 5 μm. (right) Confocal z resliced images along the white dashed lines in the maximum projection images. Scale bar, 2 μm. **f,** Quantification of the enrichment factor (I_{IN}/I_{OUT}) of Notch variants relative to the cadAJs. A box-plot showing binary localization of NΔEGF which are defined as either excluded (yellow) or enriched (orange) is shown on the right. **P < 0.01, ***P < 0.001, ns: non-significant, one-way ordinary ANOVA followed by Tukey's multiple comparison testing. **g,** Confocal *z*-resliced images showing the distribution of extracellular SNAP (purple) and intracellular mCherry (red) tags of NΔEGF relative to Ecad-AJs (green) after DAPT removal. Scale bar, 3 μm. **h,** A box-whisker plot showing Pearson correlation coefficients of extracellular-SNAP (purple) and intracellular-mCherry (red) domains relative to the cadAJs before and after DAPT washout (***P < 0.001; ns, not significant; n = 9 biological replicates; two-tailed unpaired Student's t-test). **i,** Time series of confocal z-resliced images showing the enrichment of NΔEGF (red) at the cadAJ (green) under DAPT treatment (t = 0), and the dissipation during DAPT washout (t ≥ 2). Scale bar, 3 μm. **j,** Single-cell traces showing the time-course of the decline of NΔEGF enrichment factor at the cadAJs during DAPT washout (mean ± s.e.m.; n = 4 independent single-cell experiments; see Extended Data Figure 6, d-f). **k, l,** Western blot analyses of cleaved NICD levels in the cells stably expressing N^{FL}, $N\Delta EGF_{1-25}$, NΔEGF, and NEXT. All cells were transfected with Ecad-GFP and incubated with TAPI2 for 24 hr. β-actin levels represent the loading control. A representative image of immunoblotting **(k)**, and quantification **(l)** of cleaved NICD levels. The average intensity of each NICD band relative to respective β-actin band was quantified and then normalized to that of NEXT (mean ± s.d.; n = 4 biological replicates; *P < 0.05, ****P < 0.0001, one-way ANOVA followed by Tukey's multiple comparison test). (**c, f, h**) Boxes and whiskers indicate the interquartile and the full ranges, respectively. Colored lines and (+) marks indicate median and mean, respectively.

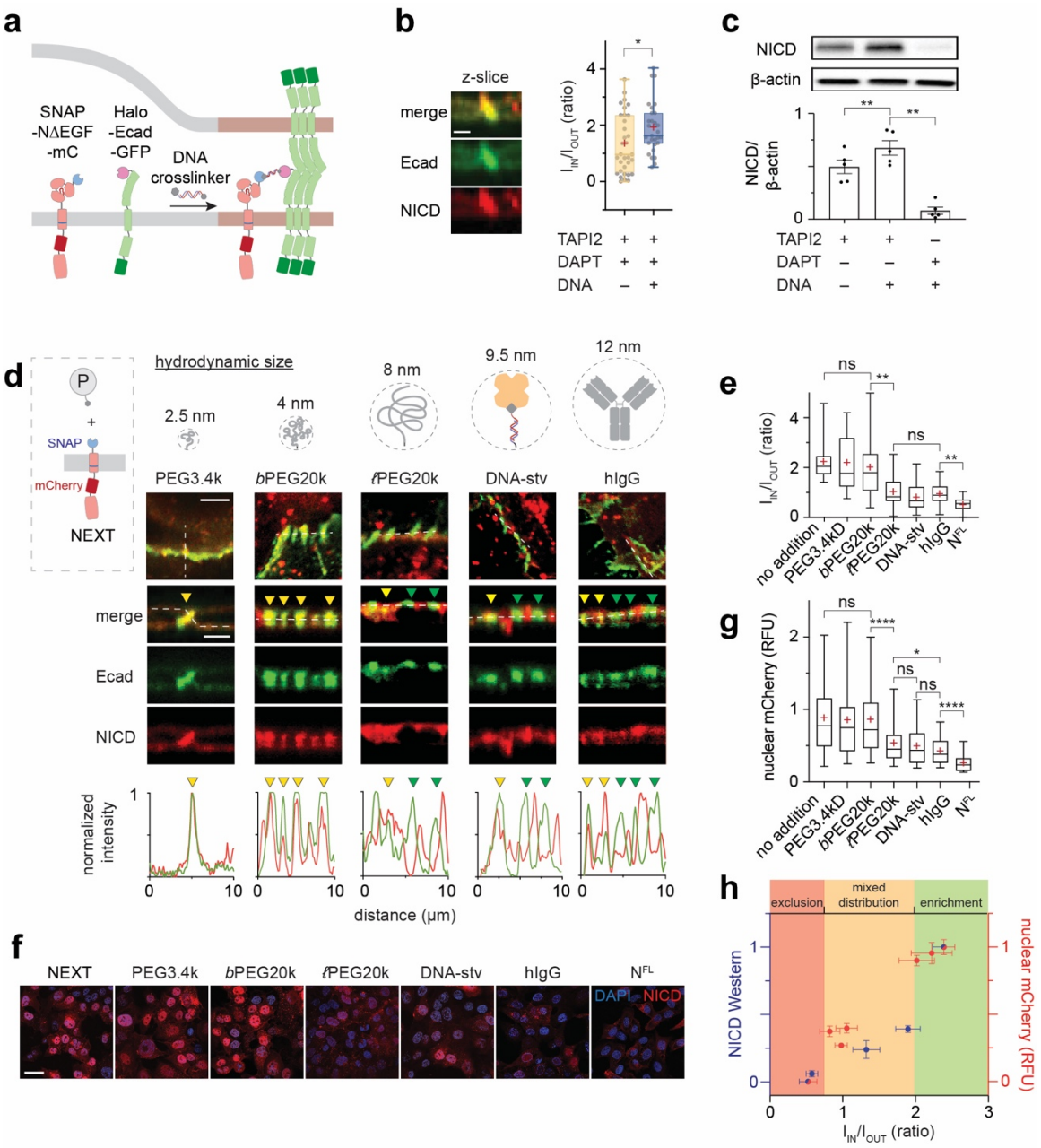

Figure 3. Spatial mutation directs Notch activation, regardless of ligand presentation or S2 cleavage. a, A schematic describing DNA-mediated crosslinking strategy to enhance NΔEGF localization at the cadAJ. **b,** Confocal z-resliced images showing intense NΔEGF fluorescence (red) enriched at the cadAJ (green) after the DNA crosslinking. Scale bar, 3 μm. Quantification of enrichment (I_{IN}/I_{OUT}) without (n = 33) with DNA crosslinker treatment (n = 29), indicating an increase in enrichment after the crosslinking (*P < 0.05; two-tailed Mann-Whitney-Wilcoxon test). **c,** Western blot analyses showing increased S3-cleaved NICD levels in the NΔEGF cells treated with the DNA crosslinker. (top) A representative gel image showing immunoblotting for NICD and β-actin. (bottom) Quantification of cleaved NICD levels. The average intensity of NICD band was normalized to that of β-actin band in each sample. (mean ± s.d.; ** P < 0.01; n = 5 biological replicates; ordinary one-way ANOVA). **d,** Spatial mutation of NEXT via chemical ligation of macromolecular pendants (denoted as P). 10 μM of BG-modified polymers or proteins were conjugated to the extracellular SNAP tag of NEXT. Cartoons depicting shape and hydrodynamic size of different pendants are shown. Confocal images showing size-dependent spatial mutation of NEXT (red) at the cadAJs (green). The top row shows maximum projection images of the cells treated with the indicated pendants. Scale bar, 5 μm. The middle row shows confocal z resliced images along the white dashed lines in the maximum projection images. Yellow and green arrowheads indicate the cadAJs enriches with and those that excludes Notch, respectively. Scale bar, 3

617 μm. The bottom row shows line profiles quantifying fluorescence signals from NEXT (red) and E-cadherin
618 (green) along the white lines in the z-resliced images. Images and line profiles are representative of n ≥
619 15 biological replicates. **e,** Quantification in I_{IN}/I_{OUT} of NEXT with macromolecular pendants (n ≥ 15). **f,**
620 Confocal fluorescence images of nuclear mCherry signals resulting from nuclear translocation of cleaved
621 NICD (red) in NEXT cells treated with macromolecular pendants. DAPI signals (blue) indicate cell nucleus.
622 Scale bar, 5 μm. **g,** Quantification of nuclear mCherry fluorescence for NEXT cells treated with the
623 pendants. Cells expressing N^{FL} were used as a negative control. Data shown are from single cells (n ≥
624 180) identified in large-area confocal images. **h,** A plot representing the NICD level of various Notch
625 variants as a function of the enrichment factor (I_{IN}/I_{OUT}, mean ± s.e.m.; n ≥ 15 biological replicates). All
626 Notch variants with different truncation length, DNA crosslinking, or pendant addition used in Figures 2
627 and 3 were included. The Notch variants showing exclusion, mixed distribution, and enrichment were
628 indicated with red, yellow, and green background colors, respectively (median ± s.e.m.; n ≥ 4 for western
629 blot for NICD levels; n ≥ 180 for nuclear mCherry fluorescence). (**e, g**) Boxes and whiskers indicate the
630 interquartile and the full ranges, respectively. Black lines and (+) marks indicate median and mean,
631 respectively. **P < 0.01; ****P < 0.001; ns, not significant; ordinary one-way ANOVA followed by Tukey's
632 multiple comparison.
633

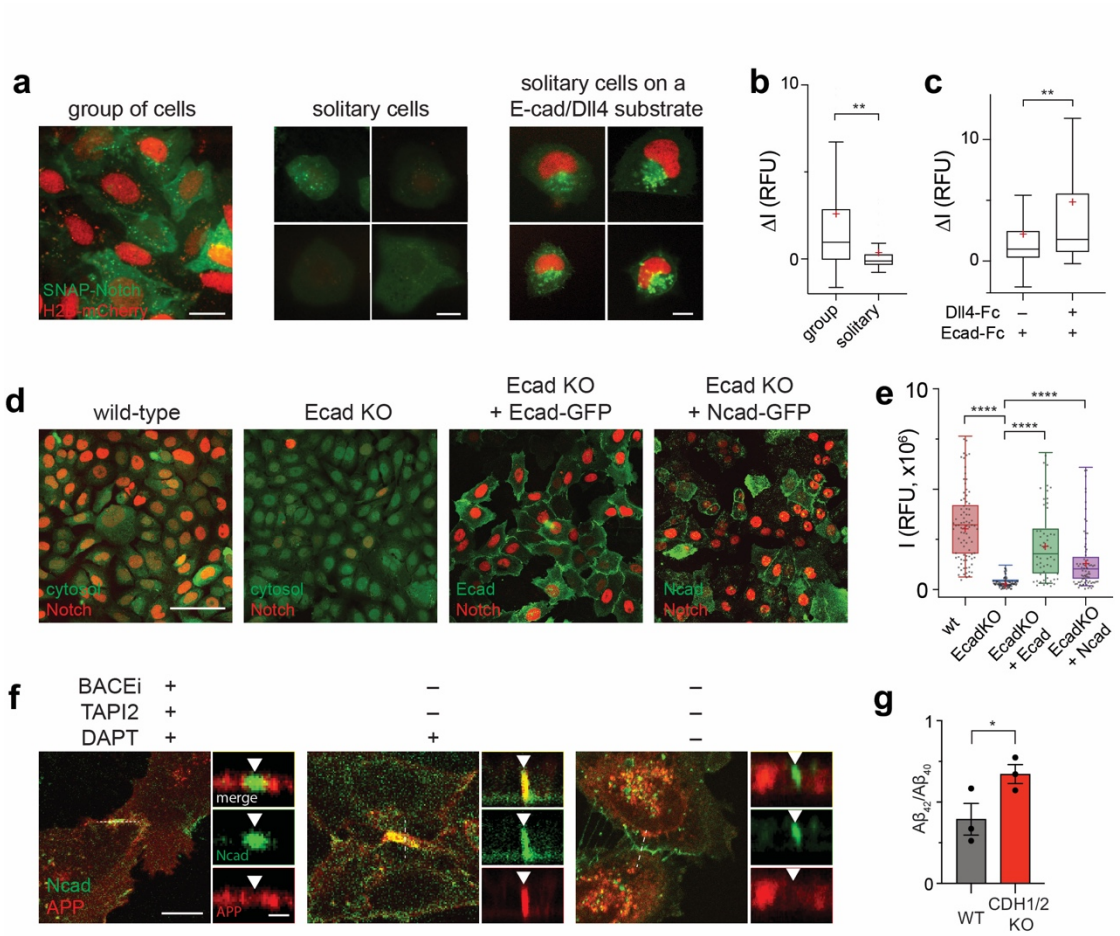

Figure 4. The cadAJ-mediated spatial switch regulates Notch and APP signaling. a, Representative fluorescence images showing Notch activation in U2OS SNAP-N^{FL}-Gal4 reporter cell lines in different cellular environments: Group of cells (left), solitary cells with no prior contact (middle), and solitary cells plated on an Ecad-Fc coated substrate (right). All cells were plated on Dll4-Fc coated substrates. Scale bars, 20 μm (see supplementary video 1, 2). **b,** Quantification of Notch activation by measuring H2B-mCherry fluorescence changes (intensity at t = 16 hr minus intensity at t = 0 hr) in cells within a group (n = 152), solitary cells (n = 50). **c,** Quantification of Notch activation in solitary cells cultured on an Ecad-Fc-coated substrate (n = 27) and those cultured without ligands (n = 27). **d,** Representative confocal images of H2B-mCherry fluorescence in U2OS SNAP-N^{FL}-Gal4 reporter cells (wt), E-cadherin knockout cells (Ecad-KO), Ecad-KO cells with recombinant E-cadherin transfection (Ecad-KO + Ecad), and Ecad-KO cells with N-cadherin transfection (Ecad-KO + Ncad). Cytosol labeled with CMFDA dye was shown for wt and Ecad-KO cells. E-cadherin and N-cadherin were shown for Ecad-KO + Ecad and Ecad-KO + Ncad cells. Scale bar, 100 μm. **e,** Quantification of Notch activation in the wt, Ecad-KO, Ecad-KO + Ecad, and Ecad-KO + Ncad cells. Data shown are from n ≥ 50 single cells analyzed from two independent experiments. **f,** (left) Confocal fluorescence maximum projection (left) and z-resliced images of U2OS cells co-expressing Ncad-mCherry (green) and APP-EGFP (red). To capture the APP intermediates, cells were cultured with a combination of α-, β-, and γ-secretase inhibitors. Scale bars, 10 μm (maximum projection) & 3 μm (inset). **g,** $A\beta_{42}/A\beta_{40}$ ratio measured by ELISA in wild-type cells or CDH1/2 KO cells (mean ± SEM, n = 3, *P< 0.05, two-tailed paired Student's t test). (**b**, **c**, and **e**) Boxes and whiskers indicate the interquartile and full ranges, respectively. Black lines and (+) marks indicate median and mean, respectively. **P < 0.01; ****P < 0.001; ns, not significant; unpaired two-tailed t test in **(b)** and **(c)**; ordinary one-way ANOVA followed by Tukey's multiple comparison in **(e)**.

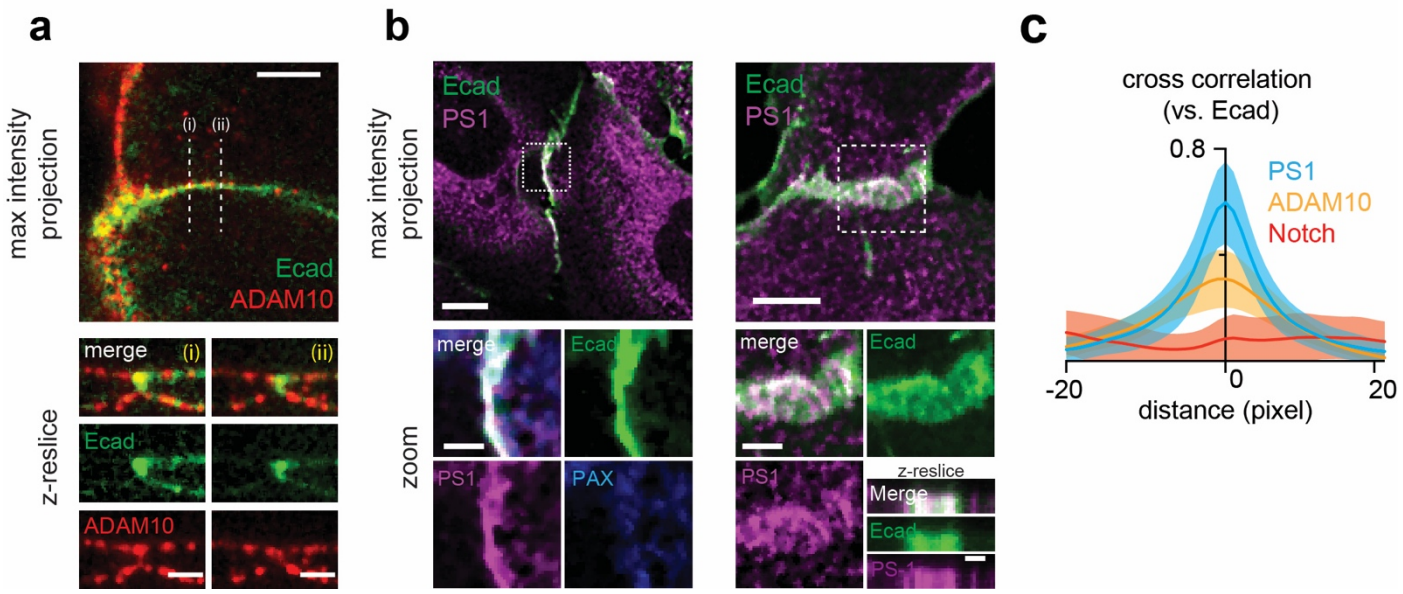

Extended Data Figure 1. Distribution of ADAM10 and γ-secretase at the cell-cell interface. a, Representative confocal fluorescence images showing ADAM10 distribution relative to E-cadherin-based adherens junction (cadAJ). U2OS cells were transfected with Ecad-GFP (green), and stained with ADAM10 antibody (red). Z-resliced images were reconstructed along the white dashed lines. Scale bars, 5 μm and 3 μm for maximum intensity projection and z-resliced images, respectively. **b,** Additional immunofluorescence confocal images showing endogenous presenilin-1 (PS1, magenta) distribution relative to cadAJs (green). Paxillin was also imaged as a negative control (blue) Scale bars, 10 μm, 3 μm, and 3 μm for maximum intensity projection, zoomed-in, z-resliced images, respectively. **c,** Cross-correlation analysis of PS1, ADAM10, and Notch distributions over E-cadherin. PS1 fluorescence intensities exhibited strong positive correlation with cadAJs, while Notch showed nearly zero correlation. ADAM10 showed a weakly positive correlation over cadAJs. The cadAJs were set as x = 0 in the analyses. The shading along the curves represent error bars (s.e.m.; n ≥ 9).

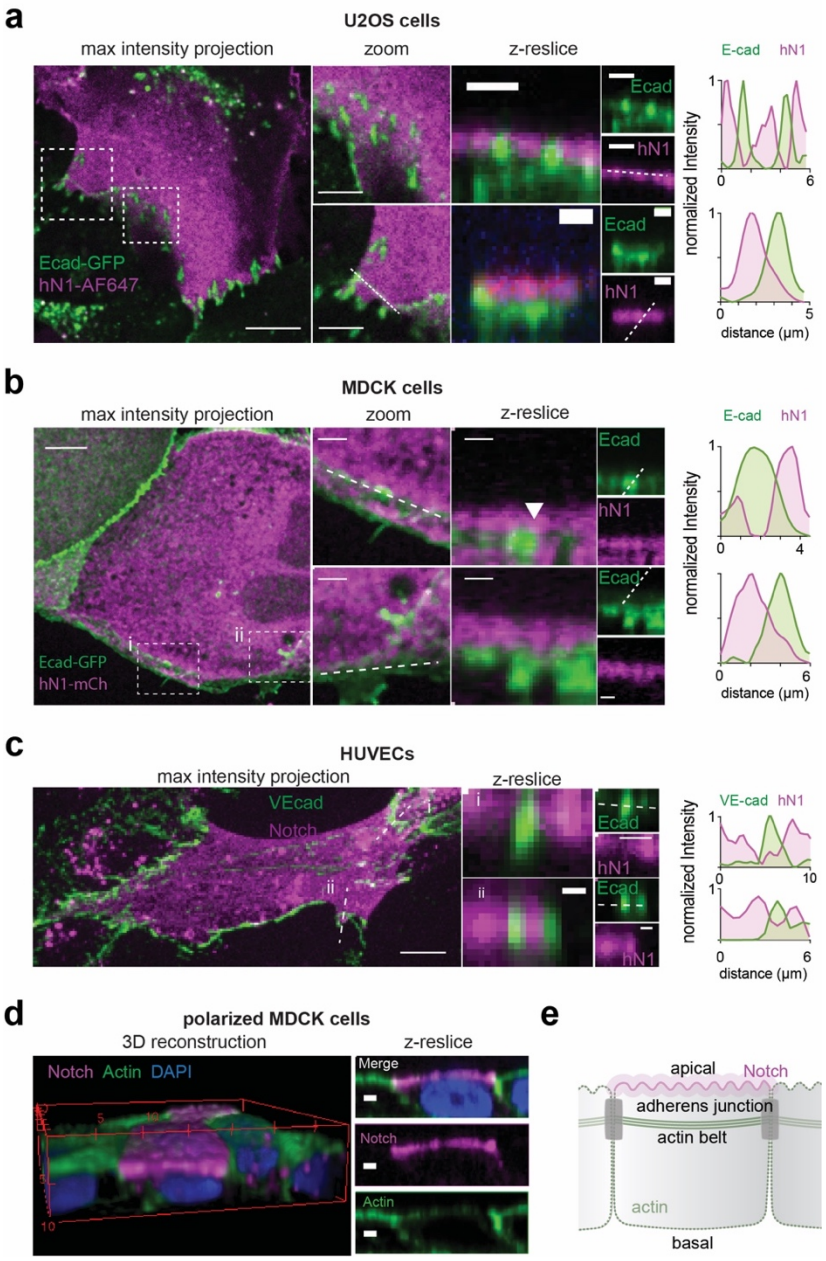

Extended Data Figure 2. Notch exclusion from cadAJs is consistent for several cadherin family proteins, host cell types, and cell polarization states. A series of cell lines including U2OS, MDCK, and HUVEC were imaged. **a, b,** U2OS (**a**) and MDCK (**b**) cells were co-transfected with plasmids encoding Ecad-GFP (green) as well as SNAP-N^{FL}-mCherry. Notch receptors were labeled with BG-Alexafluor647 (magenta). Line profiles show fluorescence signal intensities along the white lines. Scale bars 10 μm, 5 μm, and 2 μm for maximum intensity projection, zoomed-in, and z-resliced images, respectively. **c,** HUVECs were transfected with SNAP-N^{F}-mCherry and labeled with SNAP surface 647. VE-cadherin was immunostained with an anti-vascular endothelial cadherin (VE-cad) antibody. Line profiles show fluorescence signal intensities along the white lines. Scale bars 5 μm and 2 μm for maximum intensity projection and z-resliced images, respectively. **d**, Polarized MDCK cells grown on a transwell filter. Scale marked every 5 μm for 3D construction and Scale bar is 2 μm for z-resliced images. **e**, A schematic representation of Notch localization in a polarized epithelial cell.

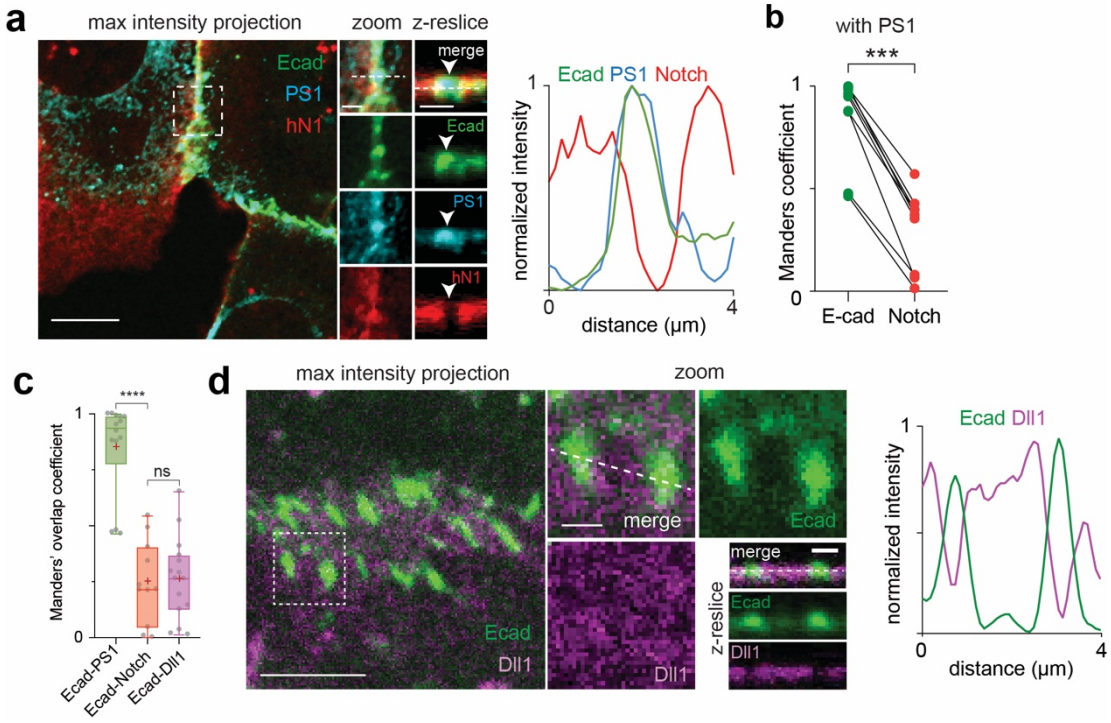

Extended Data Figure 3. Quantitative analysis of PS1, Notch, Dll distribution relative to cadAJs and additional confocal images representing their spatial distribution. a, Confocal images of U2OS cells co-expressing Ecad-GFP (green) and SNAP-N^{FL}-mCherry (red). Cells were also immunostained with anti-PS1 antibodies (cyan). Line profiles show fluorescence signal intensities along the white lines. Scale bars, 10 μm, 2 μm, and 2 μm for maximum intensity projection, zoomed-in, and z-resliced images, respectively. **b**, Paired analysis of Manders' overlap coefficients of E-cadherin and Notch signals over PS1 in multiple cells (n = 9). ***P < 0.001. **c,** Box-whisker plots showing Manders' overlap coefficients (MOCs) of PS1 (cyan), Notch (red), and Dll1 (purple) relative to cadAJs. Each dot represents the MOC of a selected cadAJ. Boxes and whiskers denote the inner-quartile and full ranges. Colored lines and (+) marks indicate median and mean, respectively (****P < 0.0001; ns, not significant; n ≥ 11; ordinary one-way ANOVA followed by Tukey's multiple comparison test). **d**, Confocal fluorescence images of U2OS cells co-expressing Ecad-GFP (green) and Halo-Dll1. Halo-Dll1 was labeled with Halo-660 dyes (magenta). Scale bars, 5 μm, 1 μm, and 1 μm for maximum intensity projection, zoomed-in, and z-resliced images, respectively.

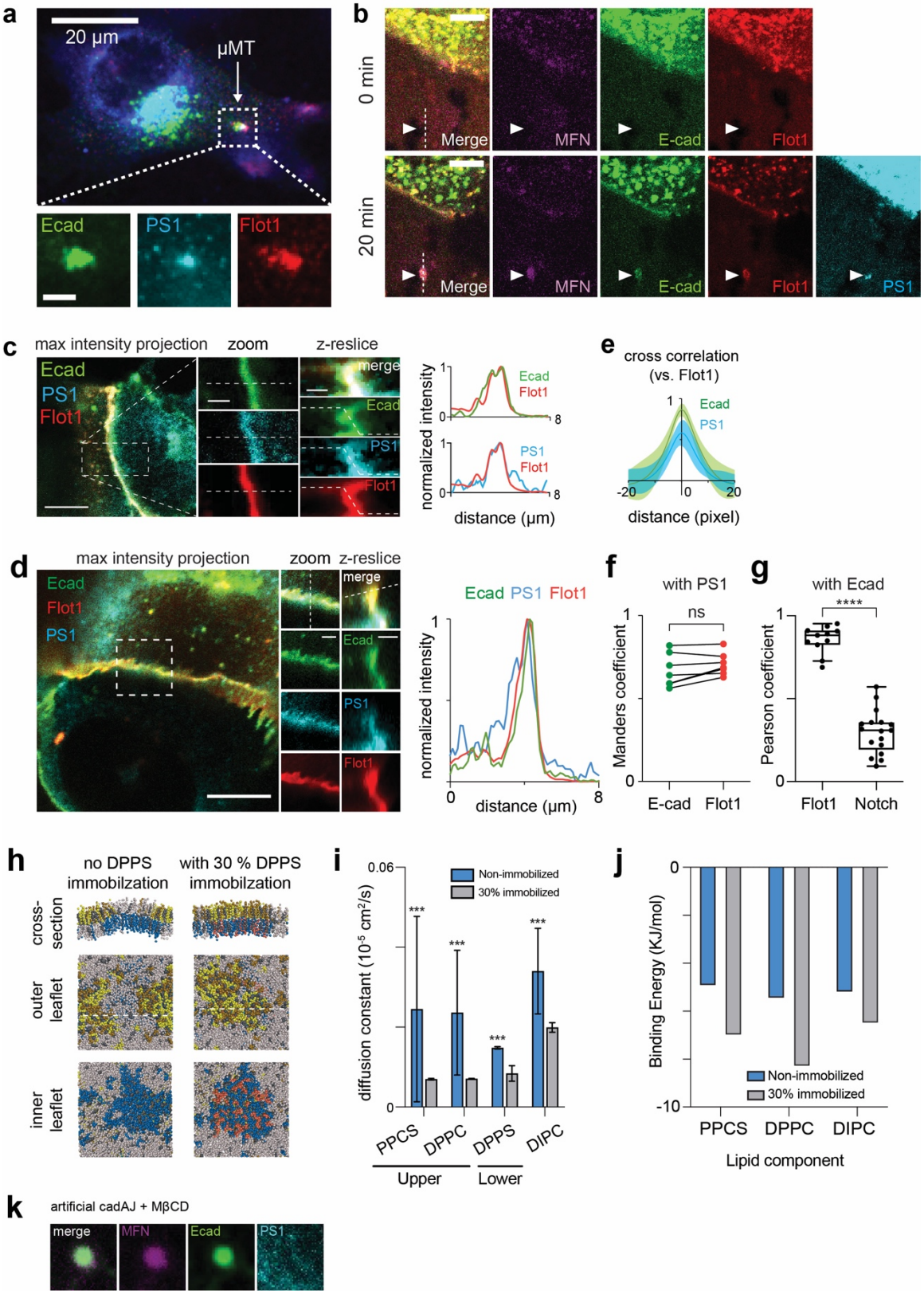

Extended Data Figure 4. Interrogation of the mechanism underlying γ-secretase recruitment into cadAJs through mechanogenetics, cell-cell cadAJ spatial mapping, molecular dynamics simulation, and cholesterol depletion experiments. a, b, Additional mechanogenetic experiments showing PS1 and Flot1 localizations at cadAJs. E-cadherin and Flot1 were labeled with fluorescent tags. Endogenous PS1 was immunostained after fixation. Scale bar, 20 μm. **c, d,** Representative confocal fluorescence images showing the PS1 and Flot1 distribution relative to native cell-cell cadAJs. (left) A

maximum projection image of merged channels. Scale bar, 10 μm. (center) Magnified images showing greater details of the boxed region. Scale bar, 2 μm. (right) Z-resliced images showing the sections of the cadAJs. Scale bar, 2 μm. Line profiles of fluorescence signals from E-cadherin, PS1, and Flot1 along the white dashed lines in the z-resliced images. **e,** Cross-correlation analysis of E-cadherin and PS1 over Flot1. Both Flot1 and PS1 fluorescence intensities exhibited strong positive correlation with the cadAJ. The shades along the curves represent error bars (s.e.m.; n = 7). **f,** Manders' overlap coefficients of E-cadherin and Flot-1 signals over PS1. Two-tailed paired Student's t test, ns: not significant. **g,** Quantitative assessment of Flot1 and Notch colocalization with E-cadherin. Pearson correlation coefficient is shown. Each circle is the score of a single cadAJ. Overlaid are box and whisker plots. **** $P<0.0001$. Two-tailed unpaired Student's t test. **h,** Snapshot images of coarse-grained MD simulation of a lipid bilayer comprising of 1,2-dilinoleoyl-sn-glycero-3-phosphocholine (DIPC; gray), 1,2-dipalmitoyl-sn-glycero-3-phosphocholine (DPPC; yellow), N-palmitoyl-O-phosphocholineserine (PPCS; green), 1,2-dipalmitoyl-sn-glycero-3-phosphoserine (DPPS; blue), immobilized DPPS (pink), and cholesterol (CHOL; grey). Left and right panels represent the simulation results without and with a partial (30%) DPPS immobilization, respectively. **i, j,** Diffusion coefficients (**i**) and binding energy (**j**) of individual lipid components in a lipid bilayer with or without a partial (30%) DPPS immobilization. Both decreases in lipid diffusion and increased binding energy indicate lipid microdomain stabilization due to DPPS immobilization. **k,** Confocal fluorescence images showing PS1 distribution at an artificial cadAJ after cholesterol depletion with MβCD treatment. No PS1 recruitment was seen at the cadAJ, suggesting that γ-secretase recruitment to the cadAJ requires lipid microdomain formation at the cadAJ.

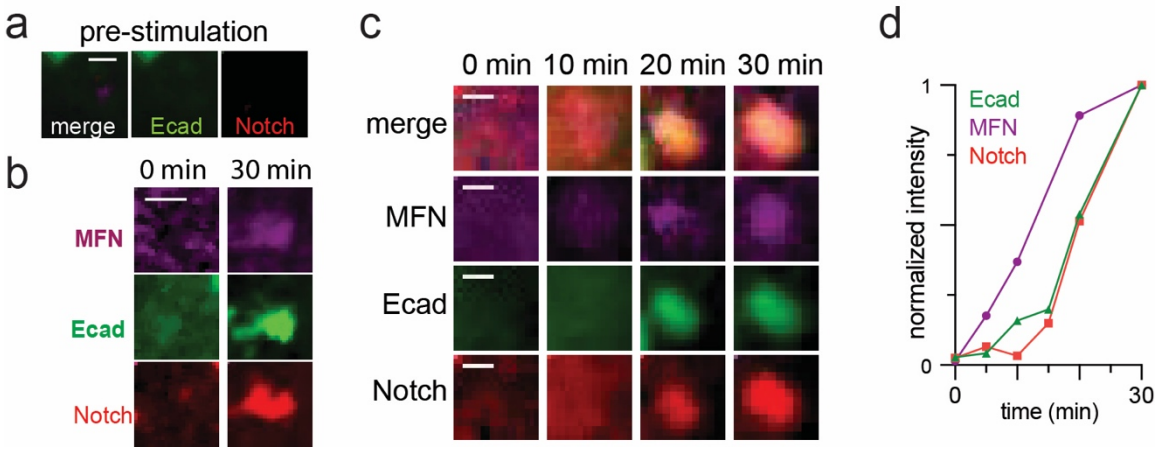

Extended Data Figure 5. Additional confocal images representing recruitment of Notch receptors to the artificial cadAJ. a, Pre-stimulation images of a subcellular locus of the cell shown in Fig. 1g. Initial dim MFN (magenta), E-cadherin (green), and Notch (red) signals were evenly distributed. Scale bar, 2 μm. **b, c,** Additional artificial cadAJs showing Notch recruitment. Time-lapse images (c) were acquired before micromagnetic tweezer (μMT) stimulation and then at 10, 20, 30 minutes of the μMT application. Gradual MFN and E-cadherin clustering were clearly seen, followed by Notch accumulation to the cadAJ. Scale bar, 2 μm. **d.** Kinetics of signal enrichments at the artificial cadAJ shown in the panel c.

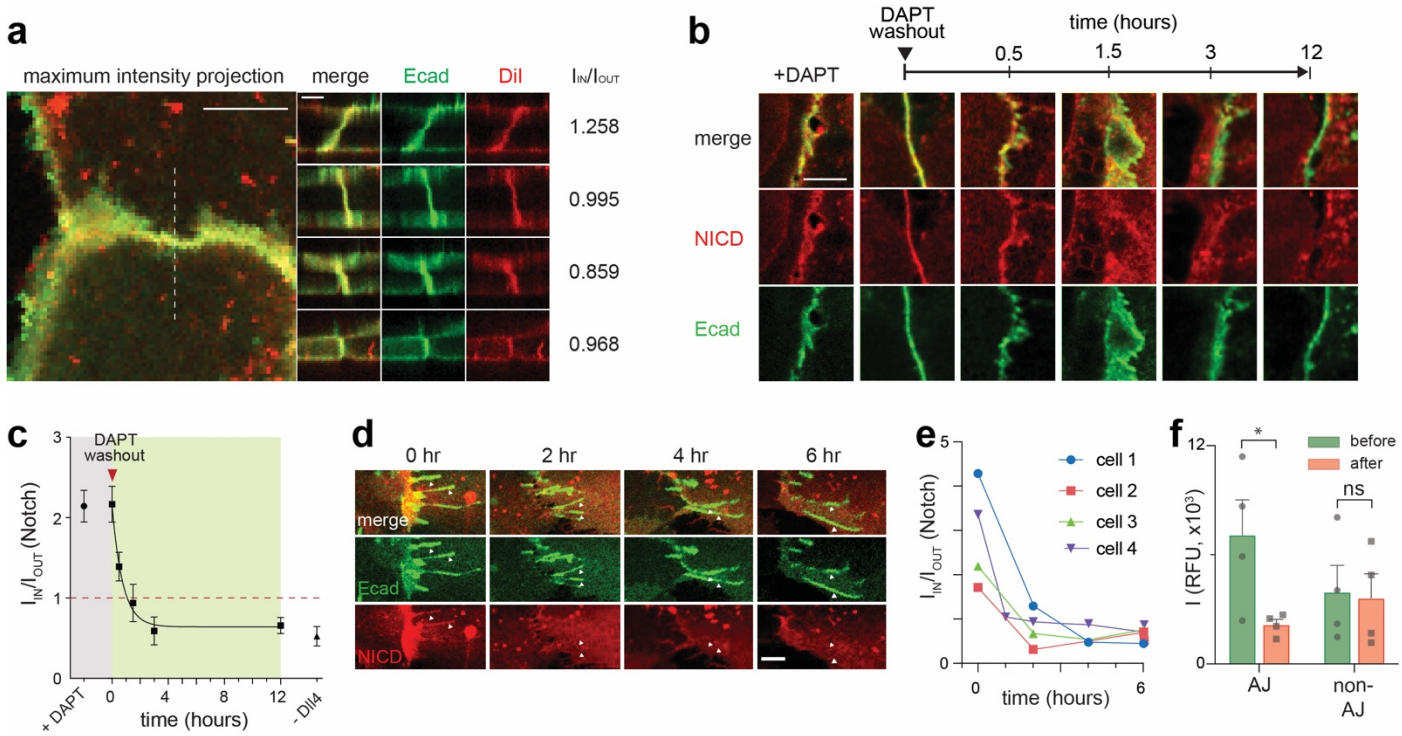

Extended Data Figure 6. Confocal images showing the gradual release of NICD from S2-cleaved Notch concentrated within cadAJs. a, Representative confocal images and enrichment factors (I_{IN}/I_{OUT}) of DiI membrane staining dye distribution relative to cadAJs. **b**, Representative time-course z-resliced images showing S2-cleaved Notch at cadAJs as a function of time after DAPT removal. The NICD signal (red) at the cadAJ gradually decreases, indicating NICD release. Images shown here are not from identical cells, but represent a general trend of NICD signal at cadAJs for each time point. **c**, Quantification I_{IN}/I_{OUT} ratio as a function of time after DAPT washout. **d-f,** Time traces of NICD release from U2OS cells expressing NΔEGF (red) and Ecad-GFP (green). **d,** Cells showing strong NΔEGF enrichment at cadAJs under DAPT treatment were chosen. DAPT was removed while keeping TAPI2 concentration constant and time series confocal images were acquired at 0, 2, 4, and 6 hrs from DAPT removal. The white arrows indicate the locations of two representative cadAJs shown and analyzed in Fig. 2i, j. **e**, Single-cell traces (n = 4) of enrichment factor. **f**, Quantification of changes in NICD signal from these four cells at the cadAJs and non-cadAJ membrane, at t = 0 (green, before washout) and t = 6 hr (red, after DAPT wash-out). CadAJs and non-cadAJ membrane were detected based on thresholding and automatic segmentation using the custom-built script. Average mCherry fluorescence signals from cadAJs and non-cadAJ membranes were also measured using the same script. Intracellular-mCherry signals significantly decreased at the cadAJs, but not at non-cadAJ membranes (* $P < 0.05$, ns: non-significant, paired two-tailed Student's t-test, n = 4). Scale bars, 5 μm.

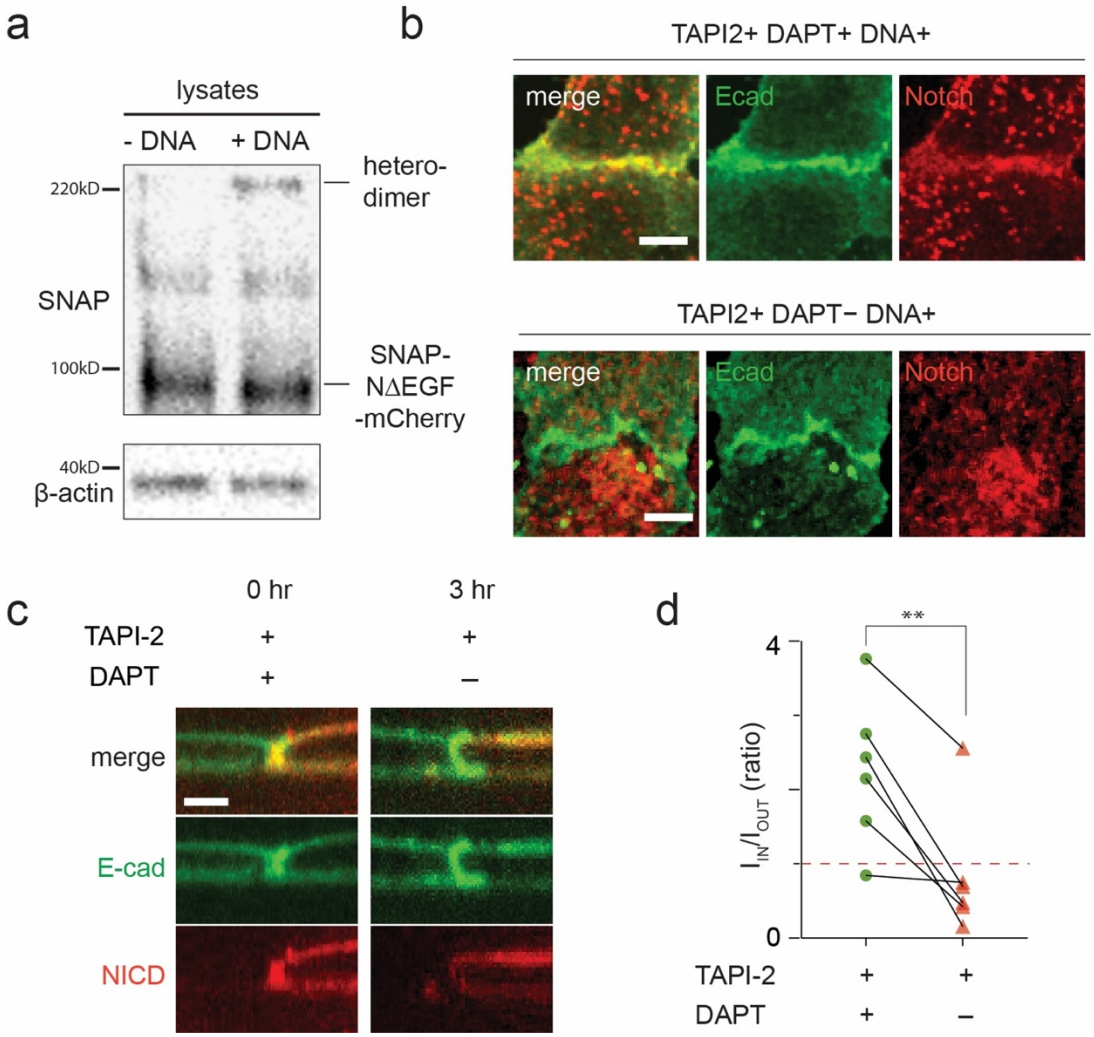

Extended Data Figure 7. Spatial mutation of NΔEGF using DNA-mediated crosslinking. a. A representative western blot of lysate from cells after 2 hr incubation with or without DNA crosslinkers. The blot was labelled with anti-SNAP and anti-β-actin antibodies. The expected mass of NΔEGF and its complex with the Notch construct and E-cadherin forming a heterodimer is 90 kD and 230 kD, respectively. β-actin detection was used to assess protein loading. Predicted bands representing Notch-E-cadherin heterodimers (heterodimer) and SNAP-NΔEGF-mCherry monomers are indicated with solid lines. Molecular weights are indicated on the left. **b.** Representative maximum intensity projection confocal images showing the distribution of NΔEGF relative to the cadAJs after crosslinking. Cells were treated with or without DAPT. Scale bar, 10 μm. **c, d,** Removal of DAPT induced S3 cleavage of NΔEGF at the cadAJs. **c,** Single-cell confocal images showing intracellular-mCherry signals at the cadAJ under DNA and DAPT treatment (left) and after washing out DAPT (right). Removing DAPT elicited a significant reduction in mCherry signal intensity from the cadAJ. Scale bar, 5 μm. **d.** Paired analysis of multiple cells expressing NΔEGF (n = 6) in enrichment factor (I_{IN}/I_{OUT}) after DAPT washout. Each dot represents I_{IN}/I_{OUT} value before and after DAPT washout from a single cell. Each line corresponds to the I_{IN}/I_{OUT} changes before and after DAPT washout in a same single cell (**P<0.01, paired two-tailed Student's t test, n = 6).

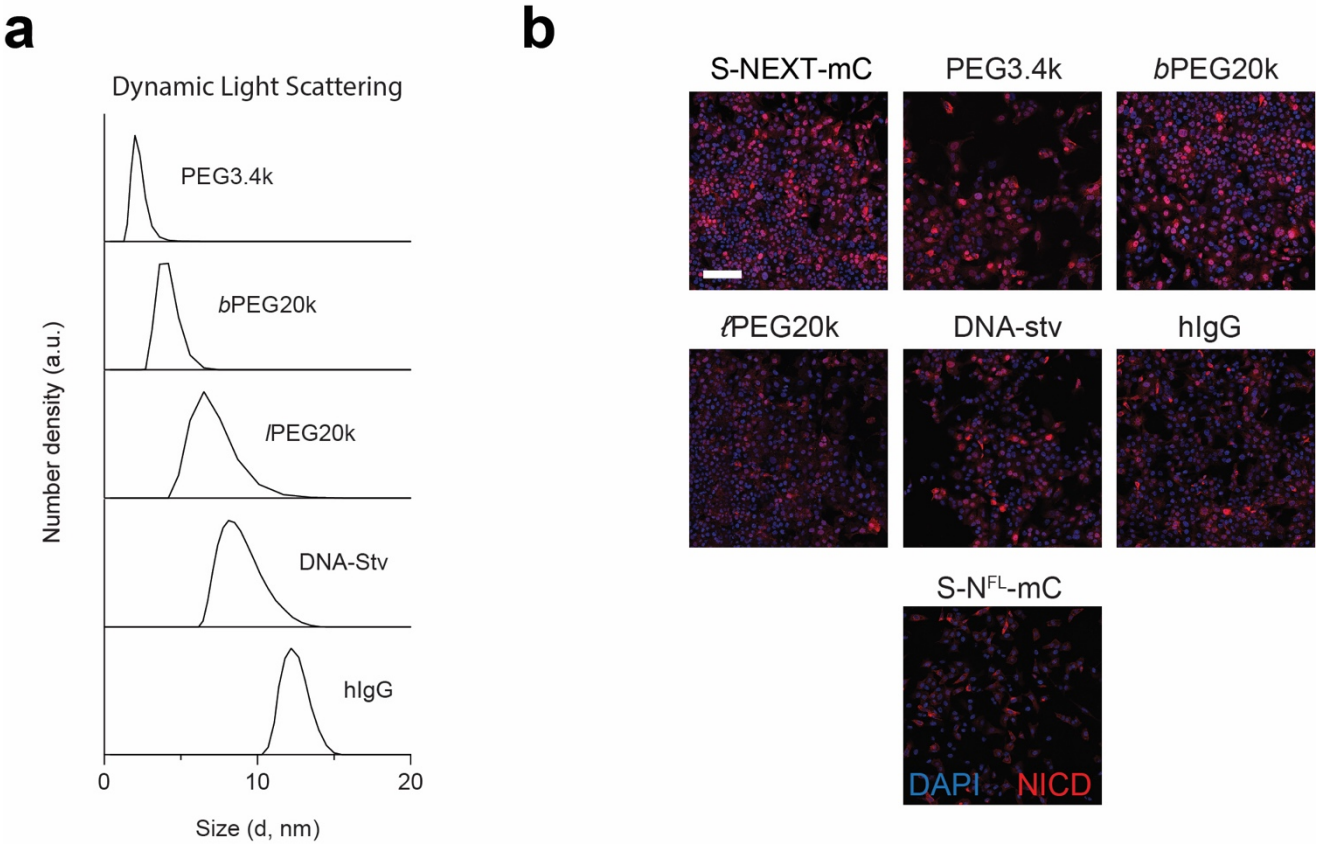

Extended Data Figure 8. Spatial mutation of NEXT using chemical ligation of macromolecular pendants. a, Dynamic light scattering spectra of BG-modified macromolecules used in the experiment to induce spatial mutation of NEXT in Fig. 3d-g. **b,** Larger area (1 x 1 mm) confocal fluorescence images shown in **Fig. 3f**. Scale bar, 200 μm.

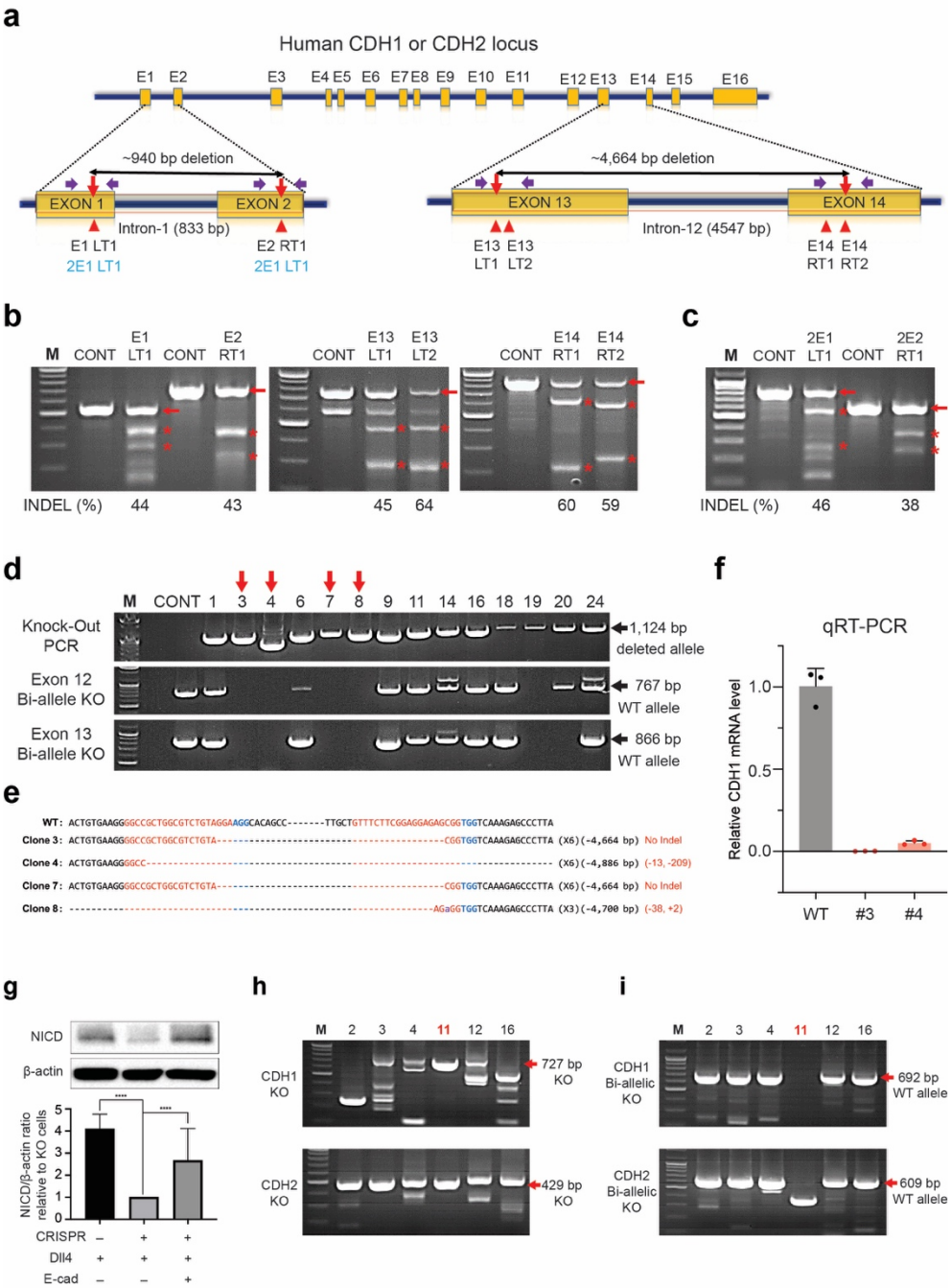

Extended Data Figure 9. Generation of U2OS SNAP-N^{FL}-Gal4 fluorescence reporter cell lines lacking E- and N-cadherins via CRISPR/Cas9. a. Schematic representation of human CDH1 gene structure and targeted segmental deletion sites. The sixteen exons are shown in orange boxes (E1-E16). Red arrowheads indicate the sgRNA-binding sites (E1LT1, E2RT1, E13LT1, E13LT2, E14RT1 and E14RT2). The targeted segmental deletion of 940bp and 4.6kb is shown with a black line with red arrow tips, respectively. Purple arrows represent PCR primers used for the T7E1 assay and detection of alleles with targeted deletions, respectively. **b, c,** T7E1 assays to evaluate the efficiency of each sgRNAs. U2OS SNAP-N^{FL}-Gal4 reporter cells were analyzed after transfection with plasmids encoding Cas9 and each sgRNA for CDH1 (**b**) and CDH2 (**c**). Mutation frequencies (indel [%]) were calculated from the band intensities. Untransfected cells were used as controls (CONT). The red arrows and asterisk indicate the uncleaved and expected cleaved position of DNA bands generated by cleavage by T7E1, respectively. M: Marker lane. **d,** Identification of clones containing the entire segmental deletion in both target alleles for selected clones. The wild-type and deleted alleles were detected by PCR using different primer pairs at exon12 and 13 target regions, respectively. The black arrows indicate the expected positions of the amplicons with wild type allele or allele with deletions. The red arrows indicate the candidate clones

802 containing the entire segmental deletion in both target alleles. **e,** Sanger sequencing of the CDH1 wild-
803 type (wt) allele and alleles containing deletions of the segmental CDH1 gene. Cas9 recognition sites are
804 shown in red and the protospacer adjacent motif (PAM) sequences are shown in blue bold characters.
805 Dashes indicate deleted bases. The number of occurrences is shown in the first set of parentheses (e.g.,
806 X6, X3 and X6 indicate how many times each sequence was observed). The cleavage sites are indicated
807 by red arrows. The sequence length of the consequent large deletion is shown in the second set of
808 parentheses. **f,** CDH1 mRNA expression levels in CDH1 KO clone #3 and #4 were determined using
809 qRT-PCR. CDH1 expression levels in the selected clones containing a segmental deletion were
810 quantified relative to CDH1 mRNA levels of the wild-type U2OS SNAP-N^{FL}-Gal4 cells. Clone #3 was used
811 for subsequent experiments. **g,** Western blot analyses of cleaved NICD levels in the U2OS SNAP-Notch-
812 Gal4 reporter cells (wt), Ecad-KO, and Ecad-KO cells with recombinant E-cadherin transfection (Ecad-
813 KO + Ecad). (top) A representative image of immunoblotting. (bottom) Quantification of cleaved NICD
814 levels. The average intensity of NICD bands relative to β-actin bands was quantified and then normalized
815 to that of Ecad-KO cells (mean ± s.d.; ***$P < 0.001$; $n = 5$ biological replicates; one-way ANOVA followed
816 by Tukey's multiple comparison test). **h,** PCR-based evaluation of targeted segmental deletions in double
817 KO (CDH1 and CDH2) single-cell derived clones. U2OS SNAP-N^{FL}-Gal4 cells were transfected with
818 plasmids encoding Cas9 and two sets of sgRNA pairs, each targeting CDH1 and CDH2, respectively.
819 The red arrow indicates the expected position of the amplicon from the region containing the segmental
820 targeted deletion M: Marker lane**. i,** To obtain the bi-allelic KO clones, we validated bi-allelic deletion in
821 both CDH1 and CDH2 genes from the indicated clones. The red arrows indicate the expected positions
822 of the amplicons with wild type allele or allele with deletions. Clone #11 (red color), showing bi-allelic
823 deletion of both CDH1 and CHD2, was used for further subsequent experiments. M: Marker lane**.**
824

825 **Extended Data Table 1. Cell lines used in this study.**

Cell line	Stable expression*,**	CRISPR-KO	Transient expression 1*,**	Transient expression 2*,**	Figure
Plain U2OS			Halo-Dll1	Ecad-GFP	1(b-d) EDF# 3a
			Ecad-GFP	Flot1-Halo	1(e-g) EDF 3(d-f)
			SNAP-Ecad-GFP	Flot1-Halo	1j EDF 5(a-d)
			Ecad-GFP		EDF 1(a-c)
			APP-GFP	SNAP-Ncad	4f
T-rex U2OS (doxycycline inducible)	SNAP-N^{FL}-mCherry (N^{FL})		Ecad-GFP		1(b-d) 2(b, c) 2(k, l) 3h EDF 2a EDF 3(b,c) EDF 7(a,b)
			Halo-Ecad-GFP		1(k, l) EDF 6(a,b) EDF 8(a-d)
	SNAP-NΔEGF$_{1-25}$-mCherry (NΔEGF$_{1-25}$)		Ecad-GFP		2(e, f) 2(k, l) 3h
	SNAP-NΔEGF-mCherry (NΔEGF)		Ecad-GFP		2(e-l) 3h EDF 7(c-e)
			Halo-Ecad-GFP		3(a-c) 3h
	SNAP-NEXT-mCherry (NEXT)		Ecad-GFP		2(e, f) 2(k, l) 3(d-h) EDF 9b
	SNAP-N^{FL}-Gal4 & UAS-H2B-mCherry				4(a-e)
		Ecad	Ecad-GFP		4(d, e)
			Ncad-GFP		4(d, e)
	SNAP-N^{FL}-Gal4 & UAS-H2B-mCherry (uninduced)		APP-GFP	SNAP-Ncad	4g
		Ecad & Ncad	APP-GFP		4g
MDCK			SNAP-N^{FL}-mC	Ecad-GFP	EDF 2(b,d)
HUVEC			SNAP-N^{FL}-mC		EDF 2c

826
827 *X-Y represents a fusion protein of X with Y.
828 **X-Y-Z represents a Y protein fused with X- and Z- tag proteins at its N- and C-termini, respectively.
829 #Extended Data Figure
830
831 Abbreviations:
832 Notch receptors and ligands
833 N^{FL}: full length Notch
834 NΔEGF$_{1-25}$: Notch with EGF domain truncation from 1-25.
835 NΔEGF: Notch with complete EGF repeat domain truncation.
836 NEXT: Notch with extracellular domain truncation
837 Dll1: Delta like ligand 1

838
839 Cadherins
840 Ecad: epithelial (E) cadherin
841 Ncad: neural (N) cadhrin
842 VEcad: vascular endothelial cadherin
843
844 Amyloid precursor proteins
845 APP: amyloid precursor proteins with deletion of YENPTY motifs
846
847 Self-labeling and fluorescent protein tags
848 SNAP: SNAP tag
849 Halo: Halo tag
850 GFP: green fluorescent protein
851
852 Others
853 Flot1: flotillin 1
854 H2B: histone 2B
855 UAS: upstream activation sequence
856
857
858
859
860
861
862

863 **METHODS**

864 **Cloning, cell culture, transfection, and cell line generation**

865 *Cloning*

866 Plasmid constructs used in this study are listed in **Extended Data Table 1**. All constructs used in this
867 paper were assembled using standard restriction enzyme-based cloning, in fusion cloning, and/or Gibson
868 isothermal assembly. The maps, sequences, and construction details of all plasmids are available upon
869 request. All constructs were sequenced to confirm mutation. Complete details of all cloning procedures
870 are available upon request.

871 Flag-human Notch1 (N^{FL})-Gal4 and pGF1-UAS-H2B-mCherry were gifts from S. Blacklow (Harvard
872 University). Flag-human N^{FL}-Gal4 was provided in a Tet-ON Flp-IN vector (pcDNA5). SNAP-N^{FL}-mCherry
873 and SNAP-N^{FL}-Gal4 were constructed as previously reported[1]. All Notch1 variants with partial or full
874 extracellular domain truncation were constructed by linearizing and amplifying SNAP-hN1-mCherry
875 vector via inverse PCR while omitting the sequence corresponding the ECD truncation. Notch
876 ectodomain sequences of amino acid 23-981, 23-1426, 23-1709 were deleted for SNAP-ΔEGF_{1-25}-
877 mCherry. SNAP-ΔEGF-mCherry. and SNAP-NEXT-mCherry. respectively.

878 Ecad-GFP was purchased from Addgene (Addgene plasmid # 28009;
879 http://n2t.net/addgene:28009). SNAP-Ecad-GFP and Halo-Ecad-GFP were constructed first by
880 linearizing and amplifying Ecad-EGFP vector via inverse PCR. SNAP- and Halo-tags were then inserted
881 in frame with E-cadherin, downstream of the E-cadherin pro-peptide (amino acid #155) and upstream of
882 EGFP, using Gibson assembly (NEB). pCMV6-Flotillin-1-Halo (Flot1-Halo) was constructed by replacing
883 the myc-tag within the pCMV6-Flotillin1-myc (purchased from Origene (MR206823)) with the Halo-Tag
884 sequence in frame with Flot1 using In-Fusion cloning (Clontech). Human amyloid precursor protein1-
885 EGFP (APP-EGFP) was created by cloning human APP695 (a gift from C. Miller of King's College London)
886 into a pEGFP-N1 plasmid (Clontech). To facilitate membrane distribution mapping, all APP constructs
887 used in confocal imaging lack YENPTY motifs. $APP^{\Delta YENPTY}$-EGFP was constructed by first linearizing the
888 vector via inverse PCR, and deleting the sequence of final 15 amino acids upstream of C-terminus of
889 APP (amino acid 681-695), which includes YENPTY motif (amino acid 682-687) using Gibson assembly.

890 *Tissue culture*

891 Human U2OS cells were cultured in McCoy's 5A media supplemented with 10% heat-inactivated FBS
892 (Life Technologies) and 1% Pen-Strep (Life Technologies) and passaged with 0.05% trypsin-EDTA.
893 MDCK cells were grown in Eagle's Minimum Essential Medium (UCSF cell culture facility) supplemented
894 with 10% heat-inactivated FBS and 1% Pen-Strep. MDCKs Cells were lifted by treating for 10 minutes
895 with PBS Ca^{2+} and Mg^{2+} free with 0.05% EDTA followed by trypsinization. HUVECs were purchased from
896 ATCC (ATCC® CRL-1730™) and grown in Endothelial Cell Growth Medium-2 (EGM-2, Lonza CC-3162)
897 for up to 4 passages (0.05% trypsin-EDTA) after thawing. All cell lines were maintained at 37°C in a
898 humidified incubator with 5% CO_2 and passaged every 2-3 days, depending on confluency, using 0.05%
899 Trypsin-EDTA (UCSF cell culture facility). For polarized MDCK culture, **c**ells were for use on a transwell
900 filter (0.4 µm, collagen coated) at high density.

901 *Transfection and cell line generation*

902 All cell lines expressing recombinant proteins used in this study are listed in **Extended Data Table 1**.
903 U2OS stable cell lines were constructed from parental U2OS T-rex cell lines (Flp-IN, Tet-ON engineered
904 cell line, gift from S. Blacklow). Constructs were inserted into the engineered Flp-IN site by co-transfection
905 with a plasmid containing the Flp-recombinase (pOG44) via electroporation with the Neon Transfection
906 System (ThermoFisher) according to manufacturer's protocol (Shock Conditions: 1230V, 10ms, 4 pulses,
907 number of cells 5 x 10^6). The amount of total DNA used was 10 µg/well: 1 µg of DNA containing the
908 desired construct and 9 µg pOG44. Cells transfected with desired plasmids were incubated in a selection
909 medium containing 400 µg/mL hygromycin (Invitrogen) for at least 10 days. All cells with Notch truncation
910 and reporter were further sorted for inducible expression of Notch variants via fluorescence-activated cell
911 sorting (FACS) on a FacsAria2 (BD) by staining for the appropriate tag (SNAP or Halo) with fluorescently
912 tagged antibody. For single-cell monoclonal population establishment, fluorescently-positive bulk-sorted
913 populations were plated into 96 well plates at 0.2 cells/well by serial dilution and grown in selection

914 medium. Each clonal cell population was tested and selected based on the levels of Notch reporter
915 activity or Notch membrane expression. U2OS cells expressing recombinant proteins transiently were
916 generated by transfecting plasmids encoding desired proteins using Neon-based electroporation. Cells
917 were allowed to settle in a 6-well cell culture dish post electroporation for 6-8 hr. To remove dead cells,
918 cells were lifted and re-plated on a fibronectin-coated glass bottom dish with 1 x 10^5 cells per well density.
919 MDCK cells were plated at 70% density then transfected with N^{FL}-mCherry utilizing Lipofectamine 3000
920 (ThermoFisher) or Neon electroporation according to the manufacturer's protocol (Shock Conditions:
921 1,650V, 20ms, 1 pulse, number of cells 5 x 10^6). HUVEC cells were transfected via electroporation with
922 SNAP-N^{FL} via the BioRad Gene Pulser system (250 V, 20 ms square wave, 1x10^6 cells/mL Gene Pulser
923 Electroporation Buffer, 5 μg/mL SNAP-N^{FL}-mC). All cells transiently expressing recombinant proteins
924 were incubated for 24-48 hr from the transfection, and then used for further analyses.

925

926 **Live cell mechanogenetics experiment**

927 Mechanogenetics experiments were performed as previously described in Kwak et al., 2019 with some
928 modifications[2,3]. Monovalent magnetofluorescent nanoparticles (MFNs) were synthesized as previously
929 described[2].

930 *Micro-magnetic tweezers (μMT) set up*. The μMT was set up and aligned on the inverted microscope with
931 point-scanning confocal and total internal reflection fluorescence (TIRF) imaging capabilities (Nikon) as
932 previously described[2,3]. The needle probe – NdFeB magnet assembly was attached to the z-translation
933 stage (Sutter Instrument, MP-325) and its location was carefully aligned with the microscopic objective
934 lens while observing the dummy substrate filled with DPBS. The μMT tip was positioned at the center of
935 the objective oculus with bright-field illumination using the X-Y translation stage linked to PIMikroMove
936 (Physik Instrumente) and μManager (UCSF). Using the z translation stage, the μMT was carefully
937 lowered to set the height of the tip to 10 μm above the focal plane while recording the X-Y coordinates
938 and the z-position of the needle probe.

939 *Preparation of cells expressing recombinant Flotilin-1 for mechanogenetics experiments*. U2OS cells
940 were co-transfected with SNAP-Ecad-GFP (5 μg) and Flot1-Halo (5 μg) plasmids using Neon
941 electroporation. 24 hr later, cells were re-plated on a #1.5 glass-bottomed dish (MatTek, d = 10 mm)
942 coated with collagen at a density of 1 x 10^5 cells per dish. To fluorescently label Flot1-Halo, cells were
943 treated in a complete McCoy medium containing 3.5 μM cell membrane permeable Halo-ligand 660 dye
944 (Promega) for 30 minutes at 37°C. Cells were washed three times with DPBS, incubated with a phenol
945 red-free complete medium, and then mechanogenetically stimulated (see below). For the cholesterol
946 depletion experiment, we also treated cells 10 mM of methyl-β-cyclodextrine (MβCD) (Sigma-Aldrich) in
947 serum-free McCoy's 5A medium for 30 min at 37°C and washed with a complete medium three times. To
948 label SNAP-Ecad-GFP with MFNs, cells were first treated with 5 μM of an oligonucleotide bearing
949 benzylguanine (BG-$T_{60}ACTG_{10}$) for 45 minutes at 37°C, washed two times with 10 ml of serum free
950 medium, and then incubated with serum-free medium containing 10 nM monovalent MFNs bearing
951 complementary sequence ($T_{60}CAGT_{10}$) and 0.5% alkali casein for 10 min at 37°C, 5% CO_2. Cells were
952 washed with 10 ml of complete medium two times, and then incubated with phenol red-free medium for
953 mechanogenetic experiments on a confocal or wide-field epifluorescence microscope.

954 *Preparation of cells expressing human Notch1 receptor for the mechanogenetic experiment*. Inducible
955 U2OS cells stably integrated with SNAP-N^{FL}-mCherry were transfected with Halo-Ecad-GFP (10 μg)
956 using Neon electroporation. 24 h later, cells were re-plated on a collagen (or fibronectin)-coated glass-
957 bottomed dish as previously described. To induce surface expression of SNAP-N^{FL}-mCherry. cells were
958 incubated with complete medium containing doxycycline (Sigma, 2 μg/mL) for 18 h. To inhibit γ-secretase
959 activity, cells were treated with DAPT (5 μM) and further incubated for 6 h. Cells were treated with 5 μM
960 of an oligonucleotide bearing chloroalkane (Cl-$T_{60}ACTG_{10}$) for 45 minutes at 37°C and labeled with MFNs
961 via the procedure described above.

962 *Mechanogenetic regulation of artificial E-cadherin junctions*. To induce MFN and hence cadherin
963 clustering, the μMT was carefully directed towards a targeted subcellular location until the tip-to-
964 membrane distance (*d*) reached 10 μm. As the tip approached the target membrane, the formation of an
965 artificial E-cadherin junctions (cadAJs) was monitored every 5 minutes. After 30 min of mechanogenetic

stimulation, the spatial distribution of MFNs, artificial cadAJs, and Flot1 (or Notch1) was monitored using time-lapse confocal fluorescence imaging. Cells were immediately fixed with 4% paraformaldehyde (Life Technologies) in DPBS for 15 minutes and washed with DPBS 3 times for 5 minutes before immunostaining.

Fluorescence labeling and Immunostaining

Fluorescence labeling of cells expressing SNAP- or Halo-tag proteins

Cells expressing SNAP- and/or Halo-tagged fusion proteins were labeled with BG- and/or chloroalkane functionalized fluorescence dyes, respectively. Dox-inducible cell lines grown on a collagen I-coated substrate were treated with doxycycline (2 µg/ml) 24 hr before labeling. Cells with transient receptor expression were labeled with dyes 48 hr post-transfection. Dye-labeling was performed by treating the cells with 5 µM fluorescence dye in serum containing media for 30 min. Cells were then washed 3 times with complete media. For live cell imaging, cells were incubated with phenol-red free complete media. For imaging of fixed cells, cells were washed with PBS, fixed with 4% PFA in PBS for 10 min, and then washed thoroughly with PBS.

Immunofluorescence staining

Fixed cells were permeabilized with 0.5% tween-20 diluted in PBS for 15 minutes, then blocked by incubation with blocking buffer (5% normal goat serum and 1% BSA in 1xPBS) for 1 hr in room temperature. For immunostaining of surface ADAM10 and ADAM17 expression, the sample were directly proceeded to blocking without a permeabilization step. Cells were incubated overnight at 4°C or 2 hr at 25°C with the primary antibodies: mouse monoclonal anti-ADAM10 (1:100; Santa Cruz Biotechnology), rabbit polyclonal anti-PS1[4,5] (1:50), mouse polyclonal anti-Paxillin (1:500; BD Bioscience), rabbit polyclonal anti-myc tag (1:200; abcam), mouse monoclonal anti VE-cadherin (1:400, BD Biosciences), and Alexa Fluor 488 Phalloidin (1:400 dillution of 200 units/mL stock ; life technologies). All antibodies were diluted in the 0.5x blocking buffer (2.5% normal goat serum and 0.5% BSA in 1xPBS). Following primary antibody incubation, cells were washed in PBS for 5 min four times and incubated with Alexa Fluor 405-conjugated goat anti-mouse (1:400, PS-1), Alexa Fluor 594-conjugated goat anti-mouse (1:400; Paxillin), Alexa Fluor 488-conjugated goat anti-mouse (1:400; VE-cadherin), and Alexa Fluor 647-conjugated goat anti-mouse (1:500, ADAM10), as appropriate. Nucleus staining was performed using Hoechst 33342 (ThermoFisher) diluted in 1xPBS (1 µg/mL) for 15 min and then washed once. Cells were incubated at room temperature in the dark for 1 hr, washed with PBS for 5 min three times, and imaged by epifluorescence, confocal, or TIRF microscopy. Epifluorescence and TIRF microscopy was performed with 60x Apo TIRF, 1.40 NA or 100x Apo TIRF, 1.49 NA oil objectives (Nikon) on a Nikon Ti Eclipse microscope equipped with OBIS solid-state lasers (488, 552, and 647 nm, Coherent Inc.), a 300W Xenon lamp (Sutter Instrument, Lambda LS), a motorized stage (ASI, MS-2000), and a temperature- and CO_2-controlled stage top incubator (Okolab, Bold Line). Unless otherwise noted, confocal microscopy was performed using Plan-Apo 60x, 1.4 NA or Plan-Apo 100x, 1.4 NA oil objectives (Nikon) on a Nikon A1R laser scanning confocal microscope. Images were acquired using Galvano scanning mode and confocal zoom of 3-4x magnification.

Monitoring dynamic spatial localization of Notch intermediates

To activate Notch, we plated cells expressing SNAP-N^{FL}-mCherry on a substrate coated with Dll4 fused with a Fc fragment (Dll4-Fc)[6]. Briefly, a glass bottom dish (Lab-Tek II Chambered Coverglass, ThermoFisher, or 7-mm glass-bottomed dish, MatTek) was coated with fibronectin (Hamster, 5 µg/ml) and Dll4-Fc (2.5 µg/ml) for 1 hr at 37°C, and washed thoroughly with 10 ml of PBS. A negative control dish was also prepared by coating it with fibronectin only. U2OS cells co-expressing SNAP-N^{FL}-mCherry and Ecad-GFP were plated and incubated with doxycycline (2 µg/mL), TAPI-2 (100 µM), and/or DAPT (5 µM). Different combinations of inhibitors were used to capture the respective intermediates (See **Fig. 2b**). After 48 hr, cells were labeled with SNAP-647 (NEB, 5 µM) and then fixed as detailed above. Inhibitor concentrations were maintained during wash and fixation steps. For DAPT washout experiments cells were plated and activated via Dll4-Fc ligand as described above. DAPT inhibitor was removed by washing

1017 in media at each time point (0, 0.5, 1.5, 3, 6, and 12 hrs). At each time point, cells were washed three
1018 times with large volumes of PBS and fixed 4% with PFA. The spatial distribution of Notch intermediates
1019 and cadAJs was monitored using spinning disk confocal fluorescence microscopy (Zeiss Cell Observer
1020 Z1), equipped with Yokagawa spinning disk and Evolve 512 EMCCD Camera (Photometrics). Images
1021 were obtained with Plan-Apo 63x, 1.4 NA or Plan-Apo 100x 1.46 NA oil objectives (Zeiss) with solid-state
1022 lasers of 405, 488, 561 nm, and 647 nm. The microscope was controlled with Zeiss Zen software (Zeiss).

1023

1024 **Plasma membrane staining using DiI dyes**

1025 U2OS cells expressing Ecad-GFP were plated on a fibronectin-coated glass bottom dish (MatTek, D =
1026 7.0 mm) at a density of 1 x 10^4 cells per dish. After 48 hr, the dish was filled with a complete McCoy's 5A
1027 medium containing 5 μM of DiI plasma membrane labeling dyes (Invitrogen) and incubated for 10 min at
1028 37°C, 5% CO_2. Cells were then washed 3 times with complete medium. The spatial distribution of cadAJs
1029 and DiI membrane staining and Ecad-GFP was monitored using spinning disk confocal microscopy. For
1030 live cell imaging, cells were incubated with phenol-red free media.

1031

1032 **Single-cell cleavage kinetics study of SNAP-NΔEGF-mC**

1033 A 6-channel μ-slide flow chamber (Ibidi, Vi 0.4) was coated with fibronectin (2.5 μg/mL) for 1 hr at 37°C
1034 and washed with PBS four times. U2OS cells co-expressing SNAP-NΔEGF-mCherry and Ecad-GFP
1035 were plated on the μ-slide flow chamber by applying 60 μL of single cell suspension at a density of 3 x
1036 10^5 cells/mL. After 3 hr, the channel was filled with a complete McCoy's 5A medium containing
1037 doxycycline (2 μg/mL), TAPI-2 (100 μM), and DAPT (5 μM). Cells were grown 48 hr in normal growth
1038 medium to reach 70-80% confluency and form cadherin adherens junctions. Cells were labeled with BG-
1039 Alexa Fluor 647 (NEB) for 30 min to stain cell surface NΔEGF. Multiple cells with stable cadAJs were
1040 identified using large-area epi-fluorescence scanning (500 μm x 500 μm), and the spatial distribution of
1041 SNAP-NΔEGF-mCherry at cadAJs under TAPI-2 and DAPT inhibition was imaged by confocal z-stack
1042 (step size = 0.2 μm, total range of z stacks = 10 μm) scanning from basal to apical membranes. Then,
1043 DAPT was removed and replaced from the cells by flowing complete medium containing doxycycline and
1044 TAPI-2 at a flow rate of 50 μl/min for 10 minutes using a syringe pump. Localization of extracellular
1045 (NECD) and intracellular (NICD) domain at the cadAJs before and during DAPT washout was monitored
1046 every 30 minutes in multiple color channels (NICD, mCherry; NECD, AF647; cadAJ, GFP) by time-lapse
1047 confocal z-stack microscopy for 12 hr. Time-lapse live cell confocal imaging was performed using a 60x
1048 Plan-Apo oil objective (NA 1.4) on a Nikon A1 laser scanning confocal microscope equipped with an
1049 environmental chamber maintaining cells at 37°C, 5% CO_2.

1050

1051 **Western Blot analysis**

1052 U2OS cells co-expressing Notch variants and Ecad-GFP (or Halo-Ecad-GFP) were incubated with culture
1053 media containing doxycycline (2 μg/mL) and TAPI-2 (100 μM) in a 6-well plate at a density of 1x10^6 cells
1054 per well. After 24 hr, cells were washed with ice-cold DPBS twice and lysed in RIPA (Invitrogen) or 1%
1055 NP-40 (Invitrogen) supplemented with complete protease and phosphatase inhibitor cocktail (100x; Cell
1056 Signaling Technology) at 4°C while gently shaking for 30 minutes. Insoluble fractions were removed by
1057 centrifugation of the cell lysates at 13,000 r.p.m. for 10 minutes. Total protein concentrations in lysates
1058 were determined by a BCA assay (Bio-Rad). 20 μg of whole cell lysates were then mixed with 4x Laemmli
1059 sample buffer (Bio-Rad) with 10% β-mercaptoethanol (BME) and heated to 95°C for 5 minutes. For
1060 western blot analysis of DNA-crosslinked heterodimers, the cell lysates were mixed with 4x Laemmli
1061 sample buffer (Bio-Rad) but no BME and were used without boiling. Samples were then loaded into a 4-
1062 15% Mini-Protein TGX precast gel (Bio-Rad) and were run at 70 V for 30 minutes and then 120 V for 45
1063 minutes. Separated proteins were transferred to a PVDF membrane using the Trans Turbo Blot system
1064 (Bio-Rad). Membranes were blocked for 1hr at room temperature in blocking solution (5% w/v nonfat dry
1065 milk in 1x TBST). The membranes were probed with anti-V1744 NICD antibody (1:1000; Cell Signaling
1066 Technology #4147), anti-SNAP (1:1000; NEB), anti-Notch1 (1:1000, Cell Signaling Technology #3447 or
1067 #4380), and anti-β-actin (1:5000; Cell Signaling Technology #4970) antibodies overnight at 4°C with

gentle rocking. The membranes were washed in TBST three times for 5 minutes and incubated with an anti-rabbit HRP conjugated antibody (Cell Signaling Technology, # at 1:2000 for NICD, mCherry, SNAP detection and at 1:10000 for β-actin detection). The target proteins were visualized by chemiluminescence using an ECL detection kit and a ChemiDoc MP imaging system (Bio-Rad). Quantification of band intensities by densitometry was carried out using the Image Lab software (Bio-Rad).

Spatial mutation of SNAP-NΔEGF-mCherry via DNA crosslinking

DNA-mediated crosslinking of *SNAP-NΔEGF-mCherry with Halo-Ecad-GFP*. DNA crosslinkers including benzylguanine (BG)- and chloroalkane (Cl) modified oligonucleotides were synthesized as previously described[2,7]. To prepare 10x crosslinking DNA stock solution, complementary BG- and Cl-modified oligonucleotides were hybridized in situ. BG-T_{10}(ACTG)$_5$ and Cl-T_{10}(CAGT)$_5$ were mixed at equimolar concentration (20 μM) in PBS, incubated at 95°C on a dry heat block for 5 min, and slowly cooled down to room temperature for 2 hr. U2OS cells co-expressing SNAP-NΔEGF-mCherry and Halo-Ecad-GFP were cultured in a 6-well plate for western blot analysis at a density of 1 x 10^6 cells per mL or in a channel of an Ibidi μ-slide for confocal imaging analysis at a density of 3 x 10^5 cells per mL. Cells were grown to 70-80% confluency for typically 24 hr, followed by overnight incubation with complete medium containing doxycycline (2 μg/mL), TAPI-2 (100 μM) and DAPT (5 μM). Cells were then serum starved with 2 ml of serum-free medium with doxycycline, DAPT, and TAPI-2 for 6 hrs. Before adding DNA crosslinkers, cells were washed and placed in 450 μl of serum-free media. 50 μl of prewarmed 10x DNA crosslinker stock solution were added to each well and incubated at 37°C. Western blot analysis to validate receptor crosslinking were performed after 30-minute incubation of the DNA crosslinkers as detailed above.

Live cell confocal time-lapse imaging. After overnight incubation with the DNA crosslinkers, imaging was performed on an inverted laser scanning confocal microscope (Nikon A1) equipped with an environmental chamber at 37°C and 5% CO_2. Images were obtained with a Plan-Apochromat 60x, 1.4 NA oil objective (Nikon) with solid-state lasers of 405, 488, 561 nm, and 647 nm. Additionally, the microscope was equipped with Ti-E Perfect Focus System (Nikon). To examine the effect of DNA-mediated crosslinking on spatial distribution of SNAP-NΔEGF-mCherry at cadAJs, multiple cadAJs were imaged in entirety from basal to apical sides for Halo-Ecad-GFP and SNAP-NΔEGF-mCherry using a 488 nm and 561 nm laser respectively, for a 12 μm range at a z-step size of 0.25 μm. To monitor dissipation of SNAP-NΔEGF-mCherry at cadAJs upon removal of DAPT inhibition, fresh phenol red-free McCoy's 5A medium containing doxycycline and TAPI-2 was introduced into the channel using a syringe pump for 10 min, and confocal *z*-stack images of the previously selected cadAJs were acquired every 30 minutes for 6 hr. Images were acquired using NIS-element software (Nikon), and image post-processing and analyses were done using Fiji/ImageJ and custom-built codes.

Spatial mutation of SNAP-NEXT-mCherry via molecular pendant addition

Synthesis of BG-modified polyethylene glycol (PEG). Amine-functionalized PEGs with different molecular weights and structures were purchased from Creative PEGWorks (NH_2-PEG3.4k), Sigma (NH_2-*b*PEG20k), and NanoCS (NH_2-*ℓ*PEG20k) and used without further purification. BG-functionalization of PEGs was performed by amine-NHS (N-hydroxysuccinimide; NEB) coupling reaction. Briefly, NH_2-PEG (0.5 μmol), BG-GLH-NHS (2.4 mg, 5 μmol), and N,N-dimethylaminopyridine (0.73 mg, 6 μmol; Sigma) were dissolved in anhydrous dimethylsulfoxide (DMSO). The mixture was reacted overnight with constant shaking. Crude products were recovered by evaporating DMSO using a Speed-Vac concentrator (Vacufuge, Eppendorf), reconstituted in 500 μl deionized water, and removed insoluble precipitates by centrifugation at 14,000 r.p.m. for 10 minutes. The BG-modified PEG was then dissolved in 200 μl in deionized water and purified by reverse-phase high performance liquid chromatography with an Agilent Eclipse XDB C-18, 5 μm, 4.6 x 250 mm column using an elution gradient of 5-75% acetonitrile in 0.02% trifluoroacetic acid.

Synthesis of BG-modified DNA-streptavidin conjugates. DNA oligonucleotides bearing biotin- and BG-functional groups were synthesized by reacting biotin-(ACTG)$_5$-NH_2 (IDT DNA) with BG-GLH-NHS as described above. Equimolar amounts of streptavidin (10 nmol) and BG-DNA-biotin (10 nmol) were

1120 dissolved in PBS (0.5 ml) for 2 hr, forming streptavidin-BG complex. The solution was concentrated to
1121 approximately 50 µl using an Amincon centrifugal filter (MWCO: 30k) and then diluted again with 0.45 ml
1122 of PBS. This concentration and reconstitution step was repeated three times to remove unconjugated
1123 DNA.

1124 *Synthesis of BG-modified human IgG*. hIgG (10 mg) and BG-GLA-NHS (0.82 mg) were dissolved in 850
1125 µl of PBS and 150 µl of anhydrous DMSO, respectively. Two solutions were mixed and reacted for 2 hr
1126 at room temperature with gentle shaking. The solution was desalted with NAP-10 and then with NAP25
1127 pre-equilibrated with PBS. The proteins were further concentrated until the final volume is 300-500 µl
1128 using Amicon centrifugal filter (MWCO: 30k). The IgG concentration was determined by measuring the
1129 absorbance at 280 nm.

1130 *Spatial mutation of SNAP-NEXT-mCherry using the BG-modified macromolecules.* U2OS cells co-
1131 expressing SNAP-NEXT-mCherry and Ecad-GFP were incubated with a complete McCoy's 5A medium
1132 containing doxycycline (2 µg/ml), TAPI-2 (100 µM), DAPT (5 µM), and respective BG-modified
1133 macromolecules (10 µM). After 24 h, cells were fixed and imaged by confocal microscopy to determine
1134 the enrichment factor of SNAP-NEXT-mCherry at cadAJs. Images were taken with a 100x objective and
1135 3x confocal zoom. 20 stage positions per each treatment were manually selected and their coordinates
1136 were stored in the computer. In each position, confocal z stacks of DAPI, Ecad-GFP and Notch-mCherry
1137 were acquired for a 12 µm range at a Z step-size of 0.25 µm to monitor the cadAJs in their entirety from
1138 basal to apical sides. To assess the levels of Notch activation, a set of identical experiment but without
1139 DAPT was performed. After 24 h, cells were fixed, stained with DAPI, and imaged by confocal microscopy
1140 to determine nuclear mCherry signals. Images were taken with a 60x objective and 1x confocal zoom. 5
1141 stage positions per each condition were selected manually. For each position, a confocal large-area scan
1142 of DAPI, Ecad-GFP, and SNAP-NEXT-mCherry was acquired for a 1 mm x 1 mm area.

1143

1144 **Plate-bound Dll4 Notch activation in high-density grouped versus solitary cells**

1145 To activate Notch, we plated SNAP-N^{FL}-Gal4 reporter cells on a substrate coated with Dll4-Fc as
1146 detailed above. Two different cell seeding densities were used: We plated cells with a density of 1 x 10^3
1147 cells per 10 mm glass-bottomed dish (MatTek, No. 1.5 glass), predominantly yielding solitary cells. We
1148 also plated cells with a density of 1 x 10^4 cells per dish, predominantly yielding high-density grouped
1149 cells.

1150 *Plate-bound E-cadherin Notch activation experiment*. Glass-bottomed dishes (MatTek, #1.5, D = 10 mm)
1151 were coated with recombinant human E-cadherin-Fc (50 µg/ml, R&D systems), recombinant human Dll4-
1152 Fc (2.5 µg/ml, Sino Biological), and fibronectin (5 µg/ml, Sino Biological) diluted in PBS for 1 hr at 37°C,
1153 and rinsed with 10 ml PBS with calcium and magnesium (UCSF cell culture facility). The U2OS SNAP-
1154 N^{FL}-Gal4 reporter cells were transfected with Ecad-GFP (10 µg) via electroporation, incubated overnight,
1155 and re-plated onto a fibronectin, E-cadherin-Fc, and Dll4-Fc coated glass-bottomed dish at a density of
1156 0.3 x 10^5 cells/ml, same as the solitary cell assay. Negative control experiment was performed with the
1157 cells plated on E-cadherin-Fc and fibronectin coated glass-bottomed dishes without Dll4-Fc coating.

1158 *Time-lapse epifluorescence imaging.* All cells were treated with 2 µg/ml doxycycline (sigma-aldrich) at
1159 the time of plating. 2 hr post-plating, cells were imaged using time-lapse microscopy. For a high-density
1160 cell seeding assay, several groups of cells having cell-cell contacts were manually identified and their
1161 coordinates were stored. For a solitary cell assay, a number of solitary cells without any prior cell-cell
1162 contact were manually identified and their coordinates were stored. While maintaining live cells on a
1163 microscope stage with a top stage incubator, time-lapse fluorescence images were acquired in GFP and
1164 mCherry channels. In each position, the microscope (Nikon) first found focuses using the Perfect Focus
1165 System (Nikon), took a DIC image, and two fluorescent images (GFP, mCherry). Epifluorescence images
1166 were obtained with an inverted microscope (Nikon, Ti Eclipse) equipped with 300W Xenon lamp (Sutter
1167 Instrument, Lambda LS), a motorized stage (ASI, MS-2000), and a temperature- and CO_2-controlled
1168 stage top incubator (Okolab, Bold Line). Images were taken with 40x (CFI Plan fluor, N.A. 1.3, Nikon)
1169 objective lens. The microscopy setup was controlled using µ-manager software.

1170

1171 **CRISPR editing to generate E-cadherin and N-cadherin knockout mutants**

1172 CRISPR/Cas9 was used to knock out E-cadherin and N-cadherin expression from U2OS SNAP-N^{FL}-Gal4
1173 reporter cells. The genes coding for the E-cadherin (CDH1) and N-cadherin (CDH2) protein from homo
1174 sapiens (gene ID: ENSG00000039068 and ENSG00000170558) were truncated by a CRISPR/Cas9
1175 paired sgRNAs excision strategy[8,9] For the fragment deletion of genomic DNA, we used a pair of gRNAs
1176 against the target locus of CDH1 (Exon 1 & 2 (940bp deletion) or 13 & 14 (~4712bp deletion) (**Extended**
1177 **Data Fig. 9b**) and CDH2 (Exon 1 & 2 (~29,255bp deletion) (**Extended Data Fig. 9c**) genes.

1178 *sgRNA design and expression vector cloning.* Cas9 and sgRNAs were expressed using the CMV
1179 promoter-driven Cas9-2A-mRFP-2A-Puro plasmid (hereafter, Cas9-puro vector) and the hU6 promoter-
1180 driven sgRNA plasmid (Toolgen), respectively. To design sgRNAs for fragmental deletion of target loci
1181 of genes, all candidate sgRNA target sites with a protospacer adjacent motif (PAM; 5'-NGG-3') within the
1182 coding sequence of CDH1 and CDH2 were initially identified. For efficient deletion, selected sgRNAs for
1183 the candidate target sites were evaluated with DeepSpCas9 sgRNA prediction tool
1184 (http://deepcrispr.info/DeepSpCas9/)[10]. sgRNAs with high DeepSpCas9 score were selected and sgRNA
1185 oligonucleotides annealed and cloned into the vector as previously described[11]. Sequences of the vectors
1186 and sgRNAs listed here are available upon request.

1187 *Generation of single-cell derived knock-out clones.* For CDH1 knockout, SNAP-N^{FL}-Gal4 reporter cells
1188 were transfected with plasmid mixtures containing Cas9-puro, U6-sgRNA encoding individual sgRNAs at
1189 a weight ratio of 1:2 using the Neon system. For CDH1 & CDH2 knockout, cells were transfected with
1190 plasmid mixtures containing Cas9-puro, U6-sgRNA targeting CDH1 loci, and U6-sgRNA targeting CDH2
1191 loci at a weight ratio of 1:1:1 using the Neon system. One day after transfection, puromycin was added
1192 to the culture media at a final concentration of 2.5 μg ml^{-1}. Three days after transfection, the pooled cells
1193 were analyzed for the indel efficiency of sgRNA pairs using T7E1 assay. To obtain single cell-derived
1194 clones containing the fragment deletion, we plated the cells after puromycin selection into 96-well plates
1195 at an average density of 0.25 cells/well. 14 days after plating, individual clones were isolated and
1196 analyzed using PCR and gel electrophoresis of genomic DNA to check the deletion and wild-type alleles
1197 as previously described[8]. We next sequenced the genomic DNA of the clones containing targeted
1198 deletions to check if the two cleavage sites were joined by the generation of indels. Sequencing of
1199 genomic regions including the target sequence was performed as previously described[12]. Briefly, PCR
1200 amplicons that included the junction regions of the deleted lncRNA target sites were cloned into the T-
1201 Blunt vector (Promega) and sequenced using universal M13FP or RP primers.

1202 *T7E1 assay.* The T7E1 assay was performed as previously described[8,13]. Briefly, genomic DNA was
1203 isolated using the Wizard Genomic DNA purification Kit (Promega) according to the manufacturer's
1204 instructions. The region including the target site was nested PCR-amplified using appropriate primers.
1205 The amplicons were denatured by heating and annealed to allow the formation of heteroduplex DNA,
1206 which was treated with 5 units of T7 endonuclease 1 (NEB) for 20 min at 37°C followed by analysis using
1207 2% agarose gel electrophoresis. Mutation frequencies were calculated as previously described based on
1208 the band intensities using Image J software and the following equation[14]: mutation frequency (%) = 100
1209 × (1 − (1 − fraction cleaved)$^{1/2}$), where the fraction cleaved is the total relative density of the cleavage
1210 bands divided by the sum of the relative density of the cleavage bands and uncut bands.

1211 *RT-PCR.* Total RNA was extracted from wild-type SNAP-N^{FL}-Gal4 reporter (WT) cells and knockout
1212 clonal cells using TRIzol (Ambion) or an RNeasy Kit (QIAGEN), after which complementary DNA (cDNA)
1213 synthesis was performed using a DiaStarTM RT Kit (SolGent Co., Ltd.). The synthesized cDNA was
1214 subjected to quantitative PCR (qPCR) in triplicate using an Applied Biosystems StepOnePlus Real Time
1215 PCR System with PowerSYBR Green PCR Master Mix (Applied Biosystems). Gene expression was
1216 normalized to that of the CDH1 gene in WT cells. Error bars represent the standard deviation (s.d.) of the
1217 mean of triplicate reactions. Primer sequences for qPCR are available upon request.

1218 *Notch activation assay.* WT cells, CRISPR *CDH1* knock-out cells (CDH1$^{-/-}$), *CDH1*$^{-/-}$ transfected with E-
1219 cadherin-GFP (CDH1$^{-/-}$ + E-cad), and *CDH1*$^{-/-}$ transfected with N-cadherin (CDH1$^{-/-}$ + N-cad) were plated
1220 on 8 well Nunc Lab-Tek II Chambered Coverglass pre-coated with recombinant human Dll4-Fc (2.5 μg/ml)
1221 and fibronectin (5.0 μg/ml) as previously described. All cells were plated at a density of 30,000 cells per
1222 well. After 24 hr incubation with doxycycline (2 μg/ml), cell cytoplasm and nucleus were stained with

1223 CellTracker CMFDA dye (Invitrogen) and Hoechst 33342 (ThermoFisher), respectively. The cells were
1224 then fixed with 4% PFA for 15 minutes at room temperature and proceeded to epifluorescence and
1225 confocal imaging.

1226

1227 **Aβ40 and Aβ42 ELISA**

1228 $1x10^6$ of wild-type or CDH1/CDH2 knockout cells were transfected with $APP^{\Delta YENPTY}$-EGFP (10 µg) and
1229 plated on 6-well tissue culture plate. After 48 hr incubation, cells were lysed using 100 µl of RIPA buffer
1230 supplemented with 1x protease/phosphatase inhibitor cocktail (ThermoFisher) for 10 minutes on ice. The
1231 cells were scraped off the plates using a cell scraper, and the lysates were transferred to 1.5 ml
1232 microcentrifuge tubes and incubated for 20 minutes at 4°C with gentle agitation. Lysates were centrifuged
1233 at 14,000xg 10 minutes at 4°C to remove insoluble portions, and the supernatant were transferred to a
1234 new tube and stored at -80C. Cell lysates were analyzed for Aβ40 and Aβ42 contents using Aβ ELISA
1235 kits from Invitrogen. All ELISAs were performed according to the manufacturer's protocols. Briefly, 50
1236 µl/well of samples, followed by 50 µl/well of detection antibodies, were applied to Aβ40 or Aβ42 coated
1237 96-well plate, and incubated for 3 hr at room temp with shaking at 300 rpm. After washing step, 100 µl of
1238 HRP-IgG solution was applied and incubated for 30 min at room temp with shaking. After washing step,
1239 100 µl of stabilized substrate solution was applied and incubated for 30 min at room temp with shaking.
1240 Finally, 100 µl of stop solution was applied. Absorbance at 450 nm was read and analyzed using a plate
1241 reader (Biotek Synergy 2). Wells were washed with wash buffer 4 times between each incubation step.
1242 Standard curves were generated using recombinant Aβ40 and Aβ42 provided by the manufacturer
1243 (Invitrogen).

1244

1245 **Image Processing and Analysis**

1246 *Cadherin junction colocalization analysis***.** Colocalization analysis was carried out in ImageJ, using
1247 thresholding to identify cadAJs and then applying the JACOP plugin to quantify colocalization using
1248 Pearson coefficient, Mander's overlap coefficients, and cross-correlation analysis.

1249 *Confocal 3D z-stack image processing.* Custom python code was used for automatic segmentation and
1250 junction intensity ratio analysis for Notch activation and truncation studies. Code is available at
1251 **(https://github.com/kmsouthard/JunctionAnalysis**) In brief, resliced z-stacks of cell-cell interfaces
1252 were thresholded to identify the cadAJs and membrane Notch signal. Notch membrane intensity was
1253 measured inside the junction and outside the junction for each cell forming the junction. The ratio of
1254 junctional intensity was calculated as ratio = $I_{junc}/(I_{cell1}+ I_{cell2})$ as deviations from the expected intensity at
1255 the junction is a function of the sum of each cell's expression level.

1256 *Intracellular mCherry nuclear translocation analysis.* mCherry nuclear translocation analysis was carried
1257 out in ImageJ. GFP images were used for automated identification of cell edges and segmentation of
1258 single cells. DAPI images were used for automated identification of nucleus by implementing the Otsu
1259 thresholding method. Nuclear mCherry fluorescence data was extracted from nuclear segments by
1260 calculating the integrated fluorescence within the nucleus and subtracting a background scattering
1261 signals. In Fig 3h, nuclear mCherry fluorescence intensities for NEXT cells treated with the
1262 macromolecular pendants were rescaled to make the intensity of N^{FL} and NEXT to 0.002 and 1.0,
1263 respectively, which are identical to the normalized band intensities of N^{FL} and NEXT measured by western
1264 blot.

1265 *Quantification of single-cell fluorescence*. Single-cell tracking and nuclear mCherry fluorescence signal
1266 analysis of UAS-Gal4 reporter cells were performed with ImageJ, as previously described[1,15,16].

1267 *Western blot quantification.* Quantification of band intensities by densitometry was carried out using the
1268 Image Lab software (Bio-Rad). Band intensities of NICD in each lane were normalized by band intensities
1269 of loading control, β-actin in the corresponding lane.

1270

1271 **Estimation of Protein heights**

1272 Protein heights including extended Notch height was estimated by measuring the structural size of each
1273 domain (i.e. EGF, NRR, SNAP) in Pymol (The PyMOL Molecular Graphics System, Version 2.0
1274 Schrödinger, LLC.) and then creating an additive estimate based on the number of domains in the full-
1275 length Notch construct and each Notch truncation.
1276

1277 **Molecular dynamics simulations**

1278 All MD simulations were conducted using the GROMACS package[17]. Polarized MARTINI 2.2 parameters
1279 were used for the simulations[18,19]. The system was composed of 54 PPCS, 54 DPPC, 108 DPPS, 288
1280 DIPC, 216 CHOL, and 10108 water molecules with a molar composition of lipid was
1281 CHOL:PPCS:DPPC:DIPC = 3.0 : 1.5 : 1.5 : 4.0 in upper layer and CHOL:DPPS:DIPC = 3.0 : 3.0 : 4.0 in
1282 lower layer. To create immobilized lipids, we increased the mass of the phosphorus atom within DPPS
1283 by a factor of 1,000, keeping everything else the same in the parameter file. The pressure was set at 1.0
1284 bar with a semi-isotropic parrinello-rahman coupling with compressibility 4.5 x 10^{-5} $bar^{-1}$and the
1285 temperature was set to 295 K using nose-hoover coupling. Each system was neutralized and brought to
1286 a concentration of 0.15 M with randomly placed sodium and chloride ions. We employed the LINCS
1287 algorithm to constrain to bond lengths[20]. A time step of 20 fs was used with an update of the neighbor list
1288 every 10 steps, which are typical values employed in MARTINI simulations. Each simulation was run
1289 afterwards for 12 μs, the last 3 μs of which was used for analysis. The MD simulations were analyzed
1290 using the in-built GROMACS tools. MDAnalysis libraries[21,22] were used for calculating diffusion constant
1291 of lipid component and *g_energy* was used for calculating interlayer interaction.
1292

1293 **Statistical analysis.** Statistical analysis was performed in GraphPad Prism 8.0 (GraphPad) or
1294 Microsoft Excel. Figure legends indicate all statistical tests used in the figure. Unless otherwise noted in
1295 the figure legends, statistical differences were determined using Student's t-test (two-tailed unpaired or
1296 paired t-test, depending on the experiment) when only two groups were compared or by ordinary one-
1297 way ANOVA followed by Tukey posthoc test when multiple groups were analyzed. The number of
1298 samples ('n') used for each experimental analysis is indicated in the figure legends. Sample sizes of
1299 sufficient power were chosen on the basis of general standards accepted by the field. In all cases,
1300 statistical significance was assumed for probability (P) < 0.05. *P<0.05; **P<0.01; ***P<0.001;
1301 ****P<0.0001; ns indicates when no significant difference was detected.

1302 **Data availability.** All raw images, immunoblot gel images, and analyzed data are available on request.
1303 Additional data that support the findings of this study are available from the corresponding author upon
1304 reasonable request.
1305

References for Methods

1. Seo, D. *et al.* A Mechanogenetic Toolkit for Interrogating Cell Signaling in Space and Time. *Cell* **165,** 1507–1518 (2016).
2. Kwak, M. *et al.* Small, Clickable, and Monovalent Magnetofluorescent Nanoparticles Enable Mechanogenetic Regulation of Receptors in a Crowded Live-Cell Microenvironment. *Nano Lett.* **19,** 3761–3769 (2019).
3. Kim, J.-W. *et al.* Single-cell mechanogenetics using monovalent magnetoplasmonic nanoparticles. *Nat Protoc* **12,** 1871–1889 (2017).
4. Georgakopoulos, A. *et al.* Presenilin-1 forms complexes with the cadherin/catenin cell-cell adhesion system and is recruited to intercellular and synaptic contacts. *Molecular Cell* **4,** 893–902 (1999).
5. Marambaud, P. A presenilin-1/gamma-secretase cleavage releases the E-cadherin intracellular domain and regulates disassembly of adherens junctions. *The EMBO Journal* **21,** 1948–1956 (2002).
6. Andrawes, M. B. *et al.* Intrinsic Selectivity of Notch 1 for Delta-like 4 Over Delta-like 1. *J. Biol. Chem.* **288,** 25477–25489 (2013).
7. Liang, S. I. *et al.* Phosphorylated EGFR Dimers Are Not Sufficient to Activate Ras. *Cell Rep* **22,** 2593–2600 (2018).
8. Lee, H. J. *et al.* En bloc and segmental deletions of human XIST reveal X chromosome inactivation-involving RNA elements. *Nucleic Acids Res.* **47,** 3875–3887 (2019).
9. Pulido-Quetglas, C. *et al.* Scalable Design of Paired CRISPR Guide RNAs for Genomic Deletion. *PLoS Comput Biol* **13,** e1005341 (2017).
10. Kim, H. K. *et al.* SpCas9 activity prediction by DeepSpCas9, a deep learning–based model with high generalization performance. *Sci Adv* **5,** eaax9249 (2019).
11. Ramakrishna, S. *et al.* Gene disruption by cell-penetrating peptide-mediated delivery of Cas9 protein and guide RNA. *Genome Research* **24,** 1020–1027 (2014).
12. Ramakrishna, S. *et al.* Surrogate reporter-based enrichment of cells containing RNA-guided Cas9 nuclease-induced mutations. *Nat Commun* **5,** 167 (2014).
13. Gopalappa, R., Suresh, B., Ramakrishna, S. & Kim, H. H. Paired D10A Cas9 nickases are sometimes more efficient than individual nucleases for gene disruption. *Nucleic Acids Res.* **46,** e71–e71 (2018).
14. Guschin, D. Y. *et al.* A rapid and general assay for monitoring endogenous gene modification. *Methods Mol. Biol.* **649,** 247–256 (2010).
15. Nandagopal, N. *et al.* Dynamic Ligand Discrimination in the Notch Signaling Pathway. *Cell* **172,** 1–32 (2018).
16. Sprinzak, D. *et al.* Cis-interactions between Notch and Delta generate mutually exclusive signalling states. *Nature Publishing Group* **465,** 86–90 (2010).
17. Van Der Spoel, D. *et al.* GROMACS: fast, flexible, and free. *J Comput Chem* **26,** 1701–1718 (2005).
18. de Jong, D. H. *et al.* Improved Parameters for the Martini Coarse-Grained Protein Force Field. *J Chem Theory Comput* **9,** 687–697 (2013).
19. Marrink, S. J., Risselada, H. J., Yefimov, S., Tieleman, D. P. & de Vries, A. H. The MARTINI force field: coarse grained model for biomolecular simulations. *J Phys Chem B* **111,** 7812–7824 (2007).
20. Hess, B., Bekker, H., Berendsen, H. & Fraaije, J. LINCS: A linear constraint solver for molecular simulations. *J Comput Chem* **18,** 1463–1472 (1997).
21. Michaud-Agrawal, N., Denning, E. J., Woolf, T. B. & Beckstein, O. MDAnalysis: a toolkit for the analysis of molecular dynamics simulations. *J Comput Chem* **32,** 2319–2327 (2011).
22. Chavent, M. *et al.* Methodologies for the analysis of instantaneous lipid diffusion in md simulations of large membrane systems. *Faraday Discuss.* **169,** 455–475 (2014).